

Incorporation of Heliospheric Imagery into the CME Analysis Tool for improvement of CME Forecasting

S. J. Wharton^{1,3}, G. H. Millward², S. Bingham¹, E. M. Henley¹, S. Gonzi¹, and D. R.
Jackson¹

¹The Met Office, Exeter, UK

²National Oceanic and Atmospheric Administration, Boulder, Colorado, USA

³University of Leicester, Leicester, UK

Key Points:

- Developed a new CME Analysis Tool called CAT-HI that incorporates Heliospheric Imagery from the STEREO spacecraft.
- CAT-HI could enable ensemble pruning when running ensemble forecasts for CMEs and trajectory corrections.
- CAT-HI could also be used in conjunction with a dedicated mission to L4 or L5.

This article has been accepted for publication and undergone full peer review but has not been through the copyediting, typesetting, pagination and proofreading process which may lead to differences between this version and the Version of Record. Please cite this article as doi:

10.1029/2019SW002166

Abstract

Coronal Mass Ejections (CMEs) cause the largest geomagnetic disturbances at Earth which impact satellites, wired communication systems and power grids. The CME Analysis Tool (CAT) is used to determine a CME's initial longitude, latitude, angular width and radial speed from coronagraph images. These are the initial conditions for the Wang-Sheeley-Arge (WSA) Enlil solar wind model, along with the ambient solar wind properties derived from magnetograms. However, the coronagraph imagery is limited by field of view. We have incorporated heliospheric imagery (HI) from the Solar Terrestrial Relations Observatory (STEREO) into CAT to create the CME Analysis Tool with Heliospheric Imagery (CAT-HI). These HI images have a larger field of view, allowing tracking of CMEs to greater distances from the Sun. We have compared the performances of CAT and CAT-HI by examining the expected arrival times of CMEs at the L1 Lagrange point and found them to be consistent. However, CAT-HI is advantageous because it could be used to prune ensemble forecasts and issue routine updates for CME arrival time forecasts. Finally, we discuss CAT-HI in the context of an operational mission at the L4 or L5 Lagrange points.

1 Plain Language Summary

Our sun often releases large explosions of hot charged particles. These eruptions can travel through space all the way to the Earth. Here, they can damage satellites and disrupt communication systems and power grids. Therefore, we would like to predict their arrival time accurately but currently this is difficult. At the moment, operators use a tool based on coronagraph images, which look at the atmosphere of the Sun. This allows them to see the eruptions leaving the Sun. However, coronagraphs have a limited field of view, so the operators quickly lose sight of the eruptions. In this work, we have added a new kind of imagery which directly images the eruptions in the space between the Sun and the Earth. This new tool will allow the operators to track the eruptions for longer, and to update their predictions of when they will arrive at Earth. The new tool could also be used in conjunction with a dedicated operational mission to monitor these eruptions. In summary, we think that the new tool presented in this paper could be a major advance in our ability to forecast these violent ejections.

2 Introduction

Coronal Mass Ejections (CMEs) are of the utmost importance in predicting geoeffective space weather events. In September 2017, active region AR12673 released 3 CMEs within the space of a week, along with 4 X-class solar flares and a Solar Energetic Particle event that caused a ground level enhancement [Redmon *et al.*, 2018]. These space weather effects can endanger technology and human lives. During the 2017 hurricane season, these solar flares caused a radiation blackout that impacted disaster relief efforts, and the CMEs compressed the magnetosphere sufficiently to put geosynchronous satellites in the magnetosheath. This was a rare case of intense space weather coinciding with extreme terrestrial weather. Redmon *et al.* [2018] provides a full account of this incident and its consequences. This event underlines the importance of accurate CME forecasting, the focus of this paper. CMEs are also responsible for creating Geomagnetically Induced Currents, due to the way they compress the magnetosphere [Sibley *et al.*, 2012; Pulkkinen *et al.*, 2017]. This can be damaging to electric power grids and wired communications systems.

Multiple methods have been proposed to fit CME fronts for the purposes of determining their speed. For example, these include the fixed- Φ method [Rouillard *et al.*, 2008] and the harmonic mean method [Lugaz, 2010]. Lugaz *et al.* [2012] compared these two methods and found that the harmonic mean method gave a more accurate time of arrival. Colaninno *et al.* [2013] compared six ways of fitting the CME leading edge and compared the time of arrivals of each. Howard and Tappin [2010] use their own model that accounts for the appearance of the CMEs in the images. All of these studies used Heliospheric Imager (HI) data from the Solar Terrestrial Relations Observatory (STEREO) [Kaiser *et al.*, 2008; Driesman *et al.*, 2008; Howard *et al.*, 2008]. These are white light images of CMEs and are explained more below. This study develops the CME Analysis Tool (CAT) developed by Millward *et al.* [2013] to fit the CME's leading edge visually.

Currently, the CAT is used for operational space weather forecasting at the National Oceanic and Atmospheric Administration (NOAA) Space Weather Prediction Center (SWPC) in the USA and the Met Office Space Weather Operations Centre (MOSWOC) in the UK. The goal of CAT is to determine the initial parameters of a CME at 21.5 solar radii. This is the inner boundary of the Enlil solar wind model [Odstrčil and Pizzo, 1999; Odstrčil *et al.*, 2002; Odstrčil, 2003], which can be used to estimate the time of arrival of

76 the CME at Earth. These parameters are the latitude, longitude, angular width and radial
77 speed of the CME. For operations, the CAT uses beacon-quality coronagraph images of
78 CMEs, ideally from at least three spacecraft. From 2006 to 2014, these were the Large
79 Angle Spectroscopic Coronagraph (LASCO) [Brueckner *et al.*, 1995] C2 and C3 corona-
80 graphs on the Solar and Heliospheric Observatory (SOHO) [Domingo *et al.*, 1995] and the
81 COR2 coronagraphs on the STEREO A (Ahead) and B (Behind) satellites. However, since
82 2014, contact has been lost with STEREO B so only SOHO and STEREO A are cur-
83 rently in use operationally ([https://stereo-ssc.nascom.nasa.gov/behind_status.](https://stereo-ssc.nascom.nasa.gov/behind_status.shtml)
84 [shtml](https://stereo-ssc.nascom.nasa.gov/behind_status.shtml)). Henceforth, we will only discuss the two-satellite case. Many scientific studies
85 have used the CAT to investigate CMEs [e.g., Lee *et al.*, 2015; Cash *et al.*, 2015], albeit
86 using science-quality images. Science-quality images are preferable to beacon-quality im-
87 ages due to better temporal coverage and improved detail. However, they are not available
88 in near-real time. This study uses science-quality images.

89 The CAT works by projecting a three dimensional lemniscate (teardrop shape) on
90 to the CME in corresponding two dimensional coronagraph images from the two satel-
91 lites. These images do not have to occur at simultaneous times. The lemniscate was an
92 improvement on the simpler cone model of Xie *et al.* [2004]. This model suffered from
93 a degeneracy between the half-angle and radius of the cone for halo CMEs and system-
94 atically underestimated the speed of the CMEs [de Koning *et al.*, 2012]. Using the CAT,
95 the operator can adjust the latitude, longitude, half-angle and radius of the lemniscate to
96 "lasso" the front edge of the CME as it appears in the two images. This fitting is done vi-
97 sually by the operator. The radius of the lemniscate can then be changed for subsequent
98 images to produce a CME leading edge versus time plot from which the radial velocity of
the CME can be calculated.

100 Two important assumptions of the CAT are that the initially defined latitude, longi-
101 tude and half-angle remain constant and that the CME does not accelerate. Another as-
102 sumption is that the CME has a circular front. Use of the CAT depends on the skill of the
103 human forecaster, which means the fitting process is subjective and depends on their per-
104 sonal definition of where the CME leading edge is located. Allowing the latitude, longi-
105 tude and half-angle to vary would increase the number of degrees of freedom the operator
106 has to manage when fitting the lemniscate. Using an elliptical lemniscate would introduce
107 a further three degrees of freedom (major axis, minor axis and rotation). This would make

108 the fitting intractable. Therefore, the assumptions of a constant, radially-expanding, circu-
109 lar shape are used to reduce the complexity for forecasters when using the tool.

110 These three parameters, plus the radial velocity estimate, can then be used to cre-
111 ate a "cone file". The density of the CME used in the cone file is assumed to be four
112 times greater than the background density. Changing the density is expected to impact the
113 CME arrival time but currently, we have no way to measure it so this is the assumption
114 employed. This cone file can be put into the Enlil solar wind model to understand how
115 the CMEs propagate towards Earth. Also required is the background solar wind speed,
116 which is calculated using the Wang-Sheeley-Argé (WSA) model [*Wang and Sheeley, 1990;*
117 *Argé and Pizzo, 2000; Argé et al., 2003, 2004; Sheeley Jr., 2017*]. This model uses mag-
118 netograms from the Global Oscillations Network Group [*Hill, 2018*] to calculate the solar
119 wind velocity. These two models are then combined to form WSA-Enlil. WSA-Enlil is
120 in use operationally at both SWPC [*Parsons et al., 2011*] and MOSWOC, and is used to
121 model the propagation of CMEs throughout the solar system.

122 Currently, the operational imagery is limited by the fields of view of the COR2 and
123 LASCO C3 coronagraphs on STEREO A and SOHO, respectively. These are 15 and 32
124 solar radii respectively. Therefore using CAT, we can only observe the CME from one
125 viewpoint at 21.5 solar radii. It is at this distance that multiple viewpoints are most neces-
126 sary. By contrast, the wider fields of view of the STEREO heliospheric imagers (HI-1
127 and HI-2) provide the opportunity to directly image the CMEs as they propagate through
128 the heliosphere all the way to the Earth. This cannot be done with coronagraphs. For ex-
129 ample, HI-1 has a field of view from around 15 solar radii to over 80 solar radii. Hence,
130 it is clear that using HI-1 data can address the issue of a lack of coronagraph data at 21.5
131 solar radii. Both heliospheric imagers work by detecting Thomson scattered white light
132 from the charged particles in the CME.

133 Accordingly, we have updated the CAT tool to include science-quality heliospheric
134 imagery [*Eyles et al., 2009*] from the STEREO A satellite and hence created the CME
135 Analysis Tool with Heliospheric Imagery (CAT-HI). CAT-HI uses a more complex view-
136 ing geometry than CAT did. It uses a 'camera object' in order to project the lemniscate
137 onto the HI images, which are assumed to be flat, an assumption discussed further in sec-
138 tion 3.1 and the appendix where we find it is reasonable to treat the HI-1 images as flat.
139 Estimating the CME speed using measurements extending to a greater distance from the

140 Sun will also improve the linear velocity estimation at 21.5 solar radii. The studies pre-
141 viously mentioned by *Howard and Tappin* [2010]; *Lugaz et al.* [2012]; *Colaninno et al.*
142 [2013] all employed HI data. *Harrison et al.* [2017] have already argued that HI can be
143 used to improve space weather forecasting and *Amerstorfer et al.* [2018] have performed
144 ensemble runs on CMEs using the HI data.

145 In this paper, we compare CAT-HI to the operational CAT. We assess the consis-
146 tency of the tool in initial parameter selection, the difference in field of view and pre-
147 dicted CME arrival times. Finally, we discuss how CAT-HI could be used in conjunction
148 with ensemble modeling of CMEs to prune ensembles, how it could be used to provide
149 CME trajectory corrections, and its relevance to a hypothetical operational mission at the
150 L4 or L5 Lagrange point.

151 **3 CAT-HI: CME Analysis Tool with Heliospheric Imagery**

152 **3.1 Additional Features for CAT-HI**

153 Since the loss of STEREO B, the CAT has relied only on images from SOHO and
154 STEREO A. To reflect this in CAT-HI, we have removed the STEREO B panel so only
155 two image panels remain, which can be seen in Figures 1 and 2 at the top. These can be
156 compared to a similar screenshot in *Millward et al.* [2013] of the original three-panel CAT.
157 For operational usage, the CAT uses beacon-quality coronagraph data from STEREO.
158 These files have a greater compression and poorer resolution than science-quality im-
159 ages but are available to the forecasters in near realtime. In a similar manner, CAT-HI
160 can show beacon and science quality HI-1 images, which are shown in Figures 1 and 2,
161 respectively, so the reader can see the difference. Science and beacon images are differ-
162 ent images taken at different times, hence the mismatch of ~ 1 hour between the times-
163 tamps in Figures 1 and 2 for both HI-1 and LASCO C3 images. The difference in ap-
164 pearance can also be due to differences in the image properties (e.g. image saturation).
165 Despite both Figures showing the same CME at approximately the same time, the shape
166 of the manually-fitted lemniscate is different. This is mainly because it is difficult to repli-
167 cate the CAT tool operator's subjective judgement of where the CME's leading edge is
168 on different fits of the same set of images, rather than because of the differences in qual-
169 ity between the beacon and science images. This subjectivity is one of the limitations
170 of the tool. We used science-quality data for this study as the CAT-HI tool was initially

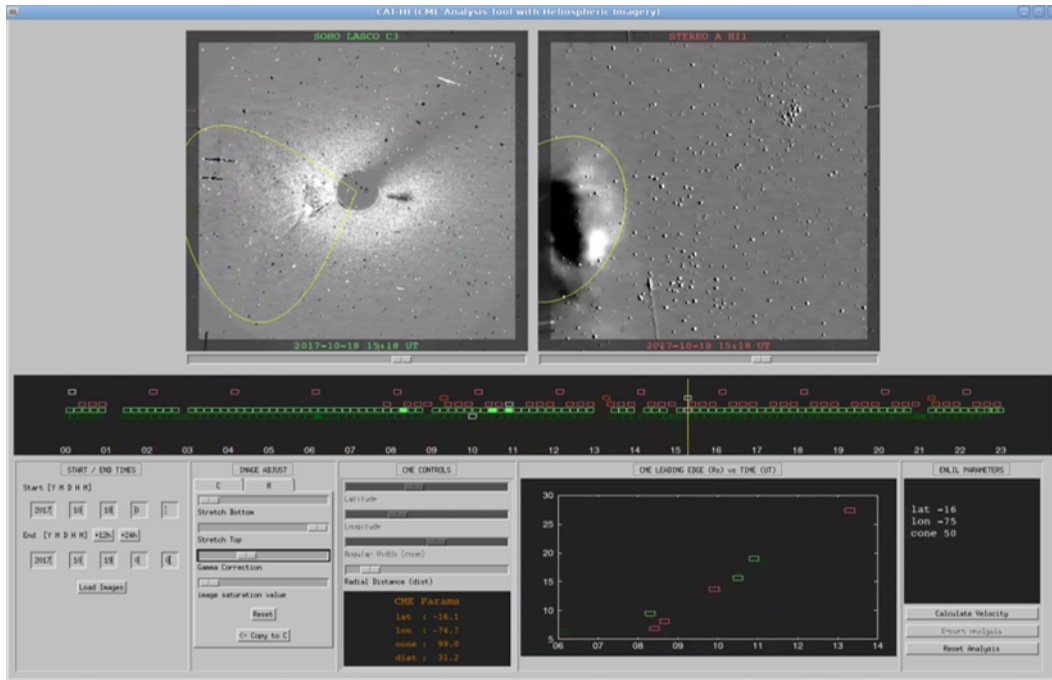
171 developed for STEREO science-quality imagery, the rationale being that a future L4/L5
172 mission would likely aim to provide the equivalent of STEREO's science-quality im-
173 agery on an operational basis. Nevertheless, Figure 1 shows that it is also possible to use
174 STEREO's beacon-grade imagery in CAT-HI. Hence, its usefulness is not contingent on
175 having science-grade imagery from any future mission. Science-quality images are also
176 taken more frequently by the HI cameras, giving better coverage of CME events for our
177 study.

178 Another complication is that because STEREO A has passed solar conjunction, it is
179 now behind the Earth in its orbit. Originally, an earthward-directed CME would propagate
180 left across the STEREO A image towards the middle panel (SOHO image), and propagate
181 right across the STEREO B image, also towards the middle panel. But because STEREO
182 A is now behind the Earth in its orbit, earthward-directed CMEs propagate the opposite
183 way across the image, away from the middle panel. The position of the two panels (after
184 removal of STEREO B) was discussed with the MOSWOC forecasters and, for consis-
185 tency, we have left the STEREO A panel on the right.

195 Another small change is that the animation panel, which allowed the user to animate
196 a series of images, has now been removed after conversation with the MOSWOC forecast-
197 ers. It was agreed this was not a useful feature so all aspects of it have been removed.

198 The main change is the introduction of HI-1 and HI-2 imagery from STEREO A. L1
199 DNS (Data numbers per second per CCD pixel) images were downloaded from the UK
200 Solar System Data Centre: <https://www.ukssdc.ac.uk/solar/>. The HI-1 and HI-2
201 images are treated equivalently to the coronagraph images; that is, as flat squares - they
202 are not projected onto the inside of a sphere. This is a reasonable assumption for HI-1,
203 which has a smaller field of view, but unreasonable for HI-2. This assumption is discussed
204 in the appendix (section 7). Hence, we only use HI-1 data in this proof of concept study.

205 Forecasters now have the option to switch the image source on the right-hand panel
206 between COR2, HI-1 and HI-2. The black imagery timeline in the middle has been up-
207 dated to accommodate this and the lemniscate scaling updated to fit the fields of view of
208 the two HI telescopes. An example of the lemniscate *lassoing* a CME in HI-1 data is
209 shown in the top right panel of Figures 1 and 2. At this point in the process, the CME
210 has evolved far from the images at which its latitude, longitude and angular width were
211 defined. This means the fit looks more ambiguous and the CMEs are fainter than in early



186 **Figure 1.** Cropped screenshot of the new interface for CAT-HI. The top left panel shows images from the
 187 SOHO LASCO C2 or C3 coronagraphs. The top right panel shows images from either the COR2 corona-
 188 graph, HI-1 telescope or HI-2 telescope on the STEREO A spacecraft. This figure shows beacon-quality
 189 HI-1 data on the right. Below is the imagery timeline, where each rectangle represents an image's universal
 190 time. Spaces represent data gaps, but these can be back-filled later if the images become available - a common
 191 occurrence in operational use. Filled in rectangles indicates which images have been used to create the range-
 192 time plot. In the bottom row, from left to right, are panels to load the images, adjust their properties (such as
 193 image saturation), sliders to determine the lemniscate properties, the plot to show leading edge of the CME vs
 194 time and the controls to determine the velocity and save the CME metadata.

212 images due to their spatial dissipation. However, we have chosen this image to showcase
 213 the propagation of the CME's radial position with time in the graph in the bottom row. It
 214 is from this graph that the radial velocity of the CME is calculated.

217 3.2 Validation of CAT-HI against the Operational CAT

218 CAT and CAT-HI were used (by the first author) to analyse the properties of 13
 19 CMEs selected from the Goddard Space Flight Centre LASCO CME catalogue (https://cdaw.gsfc.nasa.gov/CME_list/). CMEs were identified from January 2016 to
 220 October 2017 that met the following criteria: (1) were not classed as poor or very poor
 21

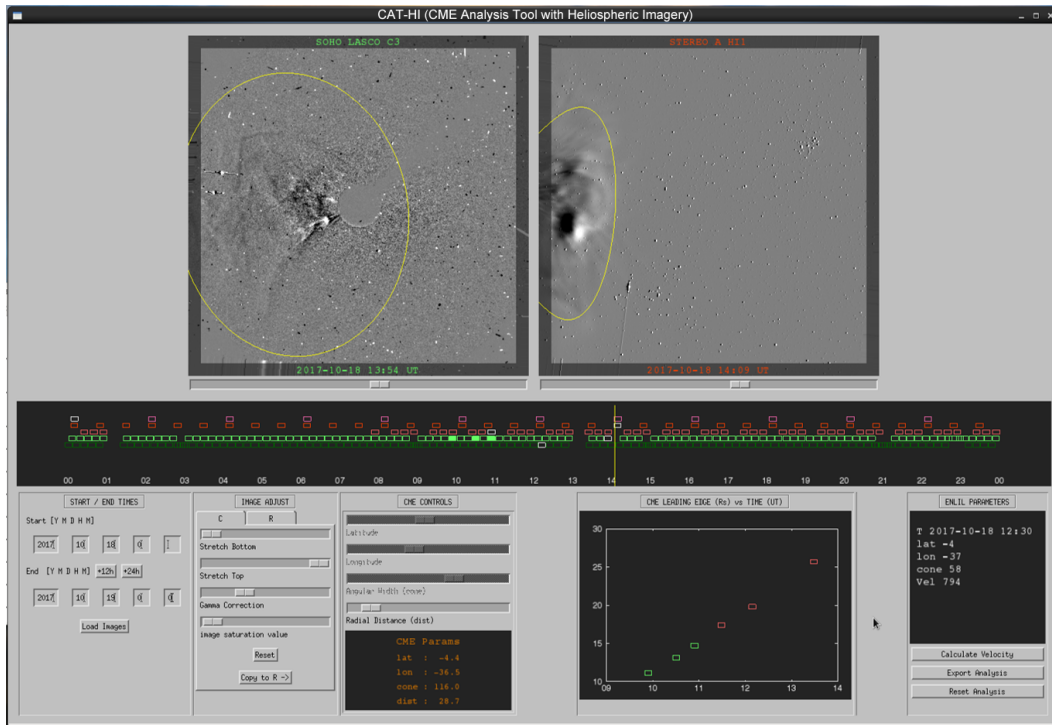
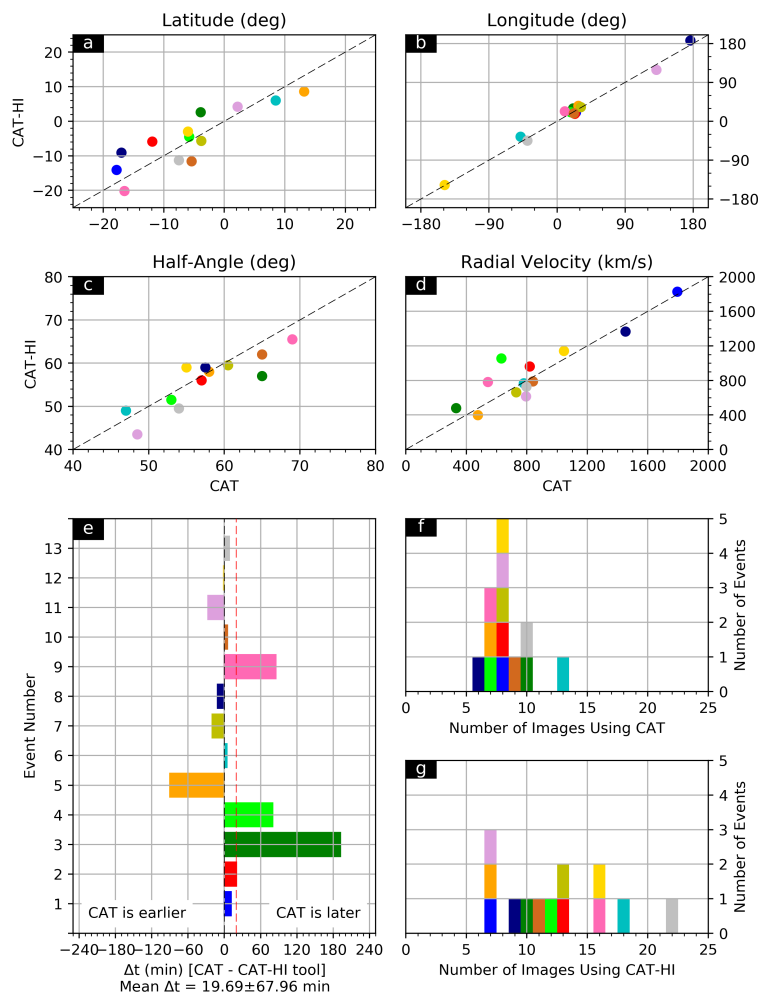


Figure 2. This screenshot shows the same CAT-HI interface as Figure 1 but with science-quality HI-1 data. Note that the science-quality HI-1 images were taken at different times, hence the different timeline.

in the remarks column, (2) were classed as Halo in the Central PA [deg] column, and (3) were clearly visible to us when loaded into the CAT tool. This gave 13 CME events across the 22 months, including the 3 CMEs described in *Redmon et al.* [2018]. During this time, STEREO A was located between -164 and -132 degrees Earth ecliptic longitude, so would be viewing Earthward CMEs from the rear. These non-ideal angles will reduce the accuracy of the lemniscate fitting.

These CMEs were first analysed with CAT then CAT-HI. There was no randomisation or blinding, which was considered acceptable as these methods would have been ineffective for the small sample size. The images analysed were running differences, where the previous image was subtracted from the current. This made it easier to observe the CME. The latitude, longitude and half angle of the CME/lemniscate were fixed using a single pair of images, usually from LASCO C3 and COR2. The fit of the lemniscate to the image was entirely visual. The radius of the lemniscate was then varied for subsequent and previous sets of images and a linear fit used to determine the radial velocity. For fitting the lemniscate in HI images using CAT-HI, the initial parameters from the COR2

237 images were kept for use on the HI images. The fit of the lemniscate to the CME was
 238 observed to worsen as the CME progressed spatially, and the fitting was stopped when it
 239 was clear the lemniscate no longer matched the CME. This may have been due to error
 240 in the initial parameter estimation or that the shape of the CMEs evolved over time away
 241 from the original fitted lemniscate. Due to the fixed shape of the lemniscate discussed in
 242 section 2, the worsening of the fit over time is inevitable.



243 **Figure 3.** Comparison of corresponding CME meta data for 13 CMEs using the CAT and the CAT-HI. (a)
 244 Latitude comparison. (b) Longitude comparison. (c) Half-angle comparison. (d) Radial Velocity comparison.
 245 (e) Relative Enlil initiation time difference between CAT and CAT-HI. (f) and (g) are histograms showing the
 246 number of images used to calculate the radial velocity with CAT and CAT-HI, respectively.

Figures 3a-d show the corresponding latitude, longitude, half-angle and radial velocity measurements from using CAT and CAT-HI. The colour of the markers corresponds to the event number, which can be found to the left of Figure 3e. The black dashed line shows the line of equivalence. This data is also summarised in Table 1.

Table 1. Initial parameters for CMEs analysed in this study. For each CME, the first entry (blue text) shows results from CAT and the second entry (red text) shows results from CAT-HI. The final column gives the event numbers and colors for each event.

Enlil Start Time	Latitude (°)	Longitude (°)	Half-Angle (°)	Velocity (km/s)	No. Images	Event
20160102 01:17	-17.8	25.0	33.5	1795	8	1
20160102 01:06	-14.1	20.4	27.5	1826	7	
20160106 18:11	-11.9	23.5	57.0	819	8	2
20160106 17:51	-5.9	17.1	56.0	960	13	
20160221 00:57	-3.9	21.3	65.0	332	10	3
20160220 21:45	2.6	29.6	57.0	478	10	
20160221 17:10	-5.8	18.1	53.0	632	7	4
20160221 15:50	-4.5	20.8	51.5	1053	12	
20160701 00:03	13.2	28.2	58.0	476	7	5
20160701 01:33	8.6	35.6	58.0	397	7	
20170419 00:28	8.5	-48.2	47.0	780	13	6
20170419 00:24	6.0	-35.9	49.0	766	18	
20170714 06:26	-3.8	31.5	60.5	730	8	7
20170714 06:46	-5.7	32.6	59.5	661	13	
20170723 07:03	-17.0	176.3	57.5	1452	6	8
20170723 07:14	-9.1	-173.2	59.0	1365	9	
20170905 02:42	-16.5	10.3	69.0	542	7	9
20170905 01:17	-20.2	22.9	65.5	781	16	
20170906 16:40	-5.4	22.2	65.0	840	9	10
20170906 16:35	-11.6	18.2	62.0	788	11	
20170910 03:10	2.2	131.4	48.5	795	8	11
20170910 03:37	4.2	118.9	43.5	614	7	
20170917 15:23	-6.0	-148.6	55.0	1045	8	12
20170917 15:24	-3.0	-147.7	59.0	1140	16	
20171018 12:09	-7.5	-39.2	54.0	797	10	13
20171018 12:01	-11.3	-45.0	49.5	726	22	

The longitude, latitude and half-angle were all consistent between the two tools. The longitude appears to be the most consistent parameter, but this is just an effect of the greater ranges on the axes. Any variation between the tools is due to uncertainty in fitting

257 the lemniscate visually. It may also be the case that a different pair of images were used
258 when performing the fits with CAT and CAT-HI. The radial velocity was higher when
259 measured by CAT-HI for low velocity CMEs but this disparity is small. Figure 3e shows
260 the difference in the Enlil start time for each event derived by the two tools. The start
261 time is when the CME reaches 21.5 solar radii, the inner boundary of the Enlil model.
262 Figure 3e shows that on average (red dashed line) the CME reaches 21.5 solar radii just
263 under 20 minutes sooner when it is measured by CAT-HI than when it is measured by
264 CAT. However, the standard deviation on this is 69 minutes, so this difference is insignif-
265 icant. All additional imagery used by CAT-HI for these events was HI-1, as the events
266 were usually too weak to be seen in HI-2. Note that these images have not been adjusted
267 to account for the spherical projection, the difference being negligible for HI-1 (see ap-
268 pendix). These results show that the inclusion of HI imagery does not make a significant
269 difference to the determination of the CME's radial velocity (at 21.5 solar radii).

270 Figures 3f and 3g show how many images were used to determine the radial velocity
271 when using the CAT and the CAT-HI, respectively. On average, the operator used ~48%
272 more images when using the CAT-HI. For two events, the operator actually used fewer im-
273 ages when using the CAT-HI than the CAT. These are events 1 and 11. For some events,
274 the CME was not clearly visible in the heliospheric imagery and no images were saved.
275 When heliospheric imagery was available, the operator sometimes used fewer images from
276 LASCO C2/C3 and COR2 when using CAT-HI than CAT.

280 For each image that is used in determining the radial velocity of a CME, the lead-
281 ing edge radius defined by the lemniscate and the universal time of the image is recorded.
282 Figure 4 shows the evolution of the leading edge of the CME in time, when using CAT
283 and CAT-HI. In order to compare the different events, the x -axis shows the time relative to
284 the Enlil start time for that event. The Enlil start time is also the time of the WSA map
285 used for the simulation. The top plot shows the leading edge position for the different
286 images when using CAT and the bottom for CAT-HI. Each triangle represents an image.
287 Straight lines have not been fitted to this data as we did not want to make the assumption
288 that the velocity was constant.

289 The bottom plot shows an increase in images taken after the Enlil start time. This
290 increase is due to the use of HI-1 imagery. The operator was able to identify the leading
291 edge of the CME in HI-1 data to over 60 solar radii in one case, but consistently above 40

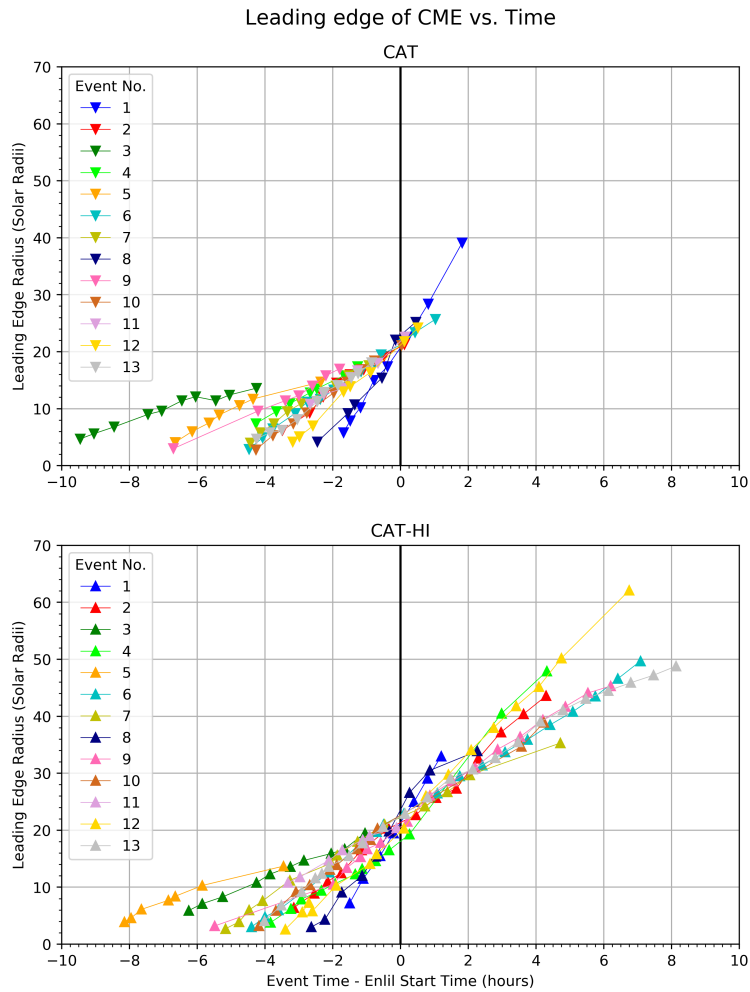


Figure 4. Leading edge radius of CME as a function of time relative to the Enlil start time. Each colour shows a different CME. Top shows results for CAT and bottom shows results for CAT-HI. The inclusion of HI-1 imagery in the latter allows fitting of a CME's leading edge further away from the Sun.

solar radii. Above these distances, the leading edge of the CME was too ambiguous and difficult to fit with the lemniscate. Note that the same image used by both tools will have different relative times, so will appear in different places on the x -axis.

Consistent measurement of the leading edge beyond 21.5 solar radii (the inner Enlil boundary) was not possible with CAT due to the limited field of view of the telescopes employed. Figure 4 illustrates the advantage of incorporating HI imagery into CAT; it allows the CME to be tracked to much greater distances from the Sun. It opens up the pos-

sibility of verifying the Enlil runs used to estimate the time of arrival of CMEs at Earth and other planets. This is discussed further in section 5.

From visual inspection, it is difficult to determine whether any of the CMEs are accelerating or decelerating. Therefore, we fitted a quadratic function (equation(1)) to the profiles in Figure 4 and performed a statistical t -test. x is the leading edge of the CME in solar radii and t is the event time minus the Enlil start time in hours, as shown in Figure 4. The constants a , b and c represent the acceleration, linear velocity and position of the leading edge at the Enlil start time, respectively.

$$x = at^2 + bt + c \quad (1)$$

Equation (1) was fitted to each profile using the method of least-squares and the best-fit values of a , b and c and their respective standard deviations σ_a , σ_b and σ_c were calculated. This was done with the Python Scipy library. The t statistic was then calculated for the acceleration (and the other parameters) and the degrees of freedom (DOF) found as the number of images minus 3, for the three parameters. The two-tailed p -value could then be calculated. The significance level was set at 5%. Any values of p less than 5% were considered significant and the CME was considered to be accelerating or decelerating.

These data are summarised in Table 2 for the acceleration parameter. Results for CAT are shown in blue and those for CAT-HI shown in red, just as in Table 1. Events with a significant p -values are shown in bold. For analysis with CAT, events 3, 5 and 7 showed a significant acceleration (or deceleration), whereas for CAT-HI, there were eight events (events 2, 4, 5, 6, 7, 10, 12, and 13). Of the significant CAT results, all three CMEs were decelerating; this was more mixed for the larger sample of significant CAT-HI results, where three CMEs were accelerating and five were decelerating. Note that of the three significant events found with CAT, only two of those were also identified as significant with CAT-HI.

These results suggest that including HI-1 images typically increases the chance of measuring a significant acceleration for the CME compared to just using coronagraph imagery. Interestingly however, the CMEs with a significant acceleration in this sample do not show a consistent behaviour, with a few accelerating and the others decelerating.

315 **Table 2.** Results of statistical test for acceleration/deceleration. For each CME, the first entry (blue text)
 316 shows results from CAT and the second entry (red text) shows results from CAT-HI. The significance level is
 317 set at 5%. Events with a significant p -value are in bold. The final column gives the event numbers and colors
 318 for each event.

Enlil Start Time	a (R_S/hr^2)	σ_a (R_S/hr^2)	t	DOF	p (%)	Event
20160102 01:17	0.298	0.182	1.633	5	16.3	1
20160102 01:06	0.155	0.152	1.019	4	36.6	
20160106 18:11	-0.375	0.150	2.490	5	5.52	2
20160106 17:51	0.115	0.051	2.241	10	4.89	
20160221 00:57	-0.180	0.063	2.867	7	2.41	3
20160220 21:45	-0.001	0.057	0.009	7	99.3	
20160221 17:10	-0.059	0.057	1.034	4	36.0	4
20160221 15:50	0.408	0.055	7.356	9	4.30×10^{-3}	
20160701 00:03	-0.402	0.038	10.689	4	4.34×10^{-2}	5
20160701 01:33	-0.270	0.047	5.802	4	4.39×10^{-1}	
20170419 00:28	-0.020	0.043	0.450	10	66.2	6
20170419 00:24	-0.050	0.014	3.655	15	2.35×10^{-1}	
20170714 06:26	-0.306	0.104	2.940	5	3.22	7
20170714 06:46	-0.101	0.019	5.405	10	2.99×10^{-2}	
20170723 07:03	0.844	0.673	1.255	3	29.8	8
20170723 07:14	-0.494	0.300	1.647	6	15.1	
20170905 02:42	0.167	0.064	2.604	4	5.98	9
20170905 01:17	0.056	0.035	1.594	13	13.5	
20170906 16:40	-0.059	0.067	0.875	6	41.5	10
20170906 16:35	-0.091	0.031	2.928	8	1.91	
20170910 03:10	0.340	0.268	1.267	5	26.1	11
20170910 03:37	-0.320	0.118	2.720	4	5.30	
20170917 15:23	-0.124	0.108	1.147	5	30.3	12
20170917 15:24	0.068	0.028	2.405	13	3.18	
20171018 12:09	0.161	0.178	0.903	7	39.7	13
20171018 12:01	-0.116	0.010	12.194	19	1.98×10^{-8}	

332 However, the sample size here is small, so we did not attempt further analysis and note
 333 that over the radial distances considered, there does not seem to be a universal tendency.

334 The increased significance of the acceleration estimates achieved via the addition
 335 of HI-1 data to CAT-HI does open the possibility of providing the acceleration of a CME
 336 to the forecaster as a secondary data product. In principle, this information could be en-
 337 tered into the WSA-Enlil solar wind model and be used to improve the time of arrival pre-

338 dictions of the CME at Earth. However, the other limitations of the tool, primarily the
 339 accuracy in fitting the lemniscate visually, result in a lot of uncertainty on the leading
 340 edge estimates. This uncertainty affects the acceleration values. We can see that the rel-
 341 ative error (σ_a/a) in Table 2 for some events can be greater than 100% (e.g. event 10 for
 342 CAT). As the acceleration is not always a reliable parameter, we judge that the benefit of
 343 including will likely be marginal in an operational context. This view takes into account
 344 the added complexity the occasional inclusion (contingent on significance) of an additional
 345 free parameter adds to the forecaster's tasks. Given this, we judge it more prudent to re-
 346 tain the current constant velocity paradigm for specification of the initial CME velocity in
 347 the WSA-Enlil-cone approach.

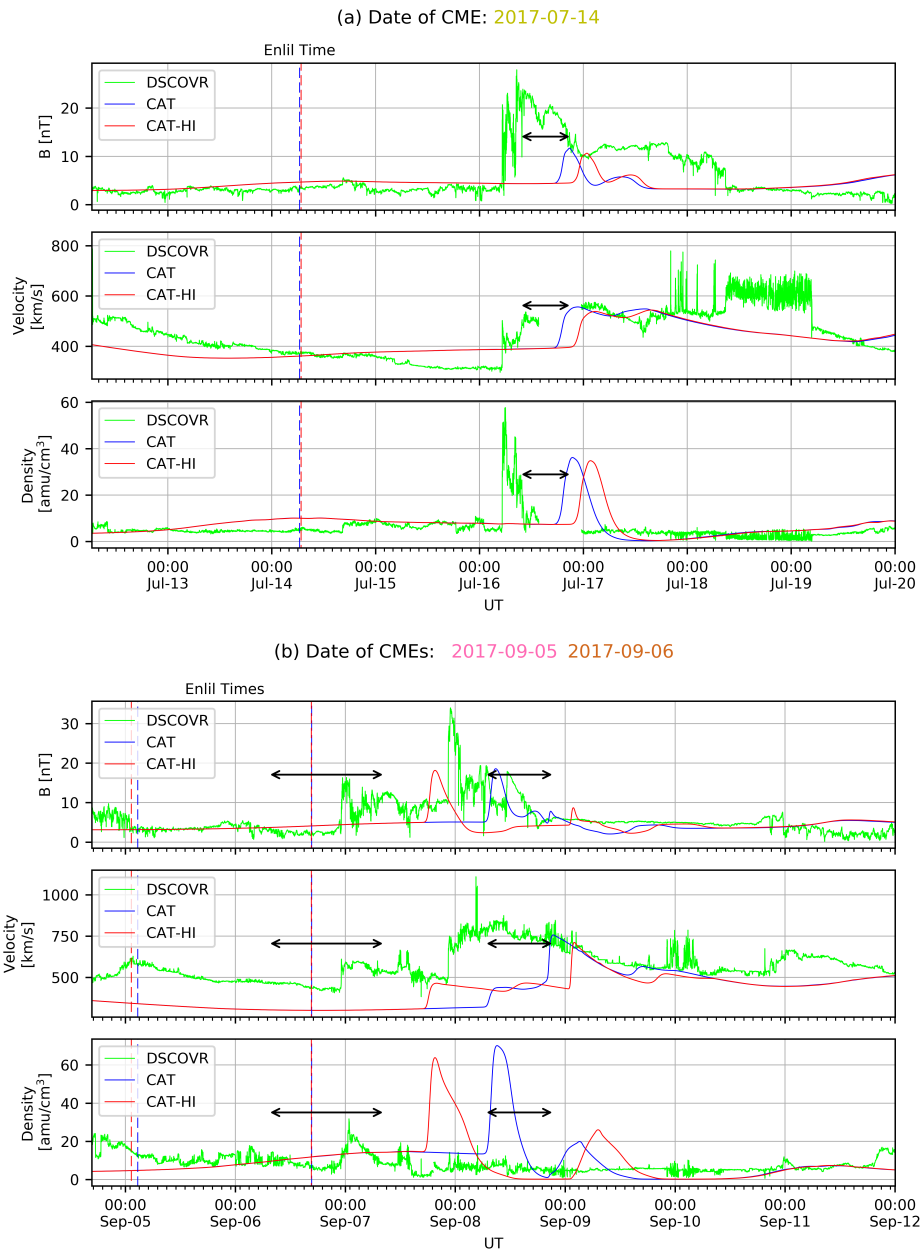
48 **4 CME Time of Arrival Predictions with CAT-HI**

49 For each of the 13 CME events, a "cone file" was made using both CAT and CAT-
 350 HI, so that WSA-Enlil runs could be performed for each tool and all CMEs. There were
 351 two instances where the CMEs were emitted in very close succession, those being two
 352 CMEs in mid February 2016 (events 3 and 4) and early September 2017 (events 9 and
 353 10). These 'double' CME events were combined into single cone files. This gave 22 WSA-
 354 Enlil runs, or 11 events. The model's predicted measurements expected at L1 could then
 355 be compared to data from the Deep Space Climate Observatory (DSCOVR) (<https://www.nesdis.noaa.gov/content/dscovr-deep-space-climate-observatory>).
 356

361 **Table 3.** Contingency table showing predictions vs. observations for each event. Top table shows predic-
 362 tions with CAT and bottom table for CAT-HI.

CAT	Forecast Hit	Forecast Miss
Observed Hit	6, 7, 9, 10, 11	13
Observed Miss	1, 2, 3, 4, 5,	8, 12
CAT-HI	Forecast Hit	Forecast Miss
Observed Hit	6, 7, 9, 10, 11, 13	-
Observed Miss	1, 2, 3, 4, 5	8, 12

63 Table 3 shows the predictions and outcomes for the 13 CMEs with regards to hitting
 364 L1. The contingency tables show prediction results using CAT and CAT-HI. The results
 65 for both tools are similar. The tables are defined very simply, as they are intended only



357 **Figure 5.** WSA-Enlil time of arrival prediction of the CME compared to DSCOVR data for CMEs in (a)
 358 July 2017 (event 8) and (b) September 2017 (events 9/10). For (a) and (b) respectively, Top: Magnetic field
 359 magnitude. Middle: Solar wind velocity. Bottom: Solar wind density. Double headed arrows show the range
 360 of predictions on the CME scoreboard (see text).

366 as a simple heuristic of whether CAT-HI yields very different results from CAT. CMEs
 367 are recorded as observed at L1 by Enlil if there is a peak in the cloud tracer parameter

[*Odstrčil and Pizzo, 2009*]. Similarly, CMEs are recorded as observed at Earth in L1 observations if there is an observed shock arrival time entry in the CCMC CME scoreboard (<https://kauai.ccmc.gsfc.nasa.gov/CMEscoreboard/PreviousPredictions/>), for entries where the CCMC CME start time at 21.5 solar radii is consistent with ours. Hits are then defined as times when CMEs are observed in Enlil and in L1 data, and so forth. Under this definition, the preliminary indications are that there is little difference between the two tools: Seven CMEs were predicted correctly for CAT, and eight for CAT-HI. For both tools, there were five false alarms.

Note these results should not be over-interpreted, as the definitions used are very simple. Specifically, we do not define a threshold for the peak in the cloud tracer parameter - peak values can range from 10^1 - 10^{-30} , where the latter are likely to be associated with "glancing blows". We have not introduced a threshold here - the presence of a peak of any magnitude is simply considered as "observed in Enlil". Likewise, we have not defined a minimum threshold for the time error (between an observation of a CME in Enlil and L1 data) required to constitute a hit. Differences can be greater than a day.

Three of the CMEs predicted to hit are presented in Figure 5. Figure 5a shows the single CME event from July 2017 (event 7) and Figure 5b shows the double CME event from September 2017 (events 9/10), the same event discussed by *Redmon et al. [2018]*. For Figure 5a and 5b, the top, middle and bottom panels show magnetic field magnitude, solar wind velocity and solar wind density, respectively. Blue lines show predictions when using CME parameters derived with CAT, red lines when using CAT-HI, and green shows data from DSCOVR. Vertical dashed lines show the Enlil start time.

For both of these events, the predicted time of arrival was late on both the CAT and CAT-HI runs. The double-headed arrows in Figure 5 describe the range of predictions made by other people from the CME scoreboard. In Figure 5a, our prediction is on the late end of this range. For Figure 5b, we have predicted both CMEs to be later than the range of predictions from the CME scoreboard. *Wold et al. [2018]* performed studies with a large number of CMEs and found on average, the WSA-Enlil prediction is 4 hours early. A study by *Möstl et al. [2014]* (not using WSA-Enlil) found a similar result and this was attributed to an overestimation of the CME speed. The CMEs analysed in Figure 5 arrived earlier than predicted, opposite to the findings of *Möstl et al. [2014]* and *Wold et al. [2018]*. Figure 5a shows that the CAT run was closer to the actual arrival time than CAT-

400 HI, whereas in Figure 5b, the CAT-HI run performed better but was still nearly 24 hours
401 late. For the double CME event, interaction between the CMEs may have complicated
402 their motion, making predicting the time of arrival more difficult in this case.

403 Consequently, the preliminary indications of this study (with small sample size and
404 without rigorous thresholds) are that incorporating the HI imagery into CAT to further
405 constrain the CME parameters introduced at the Enlil inner boundary, does not produce
406 any meaningful improvement in the resulting estimated time of arrival of CMEs using
407 Enlil. This is similar to the results of *Barnard et al.* [2017]. They used HI data and a drag
408 based model to estimate the time of arrival of CMEs but found that the HI data did not
409 improve the predictions compared to the SWPC prediction.

410 However, the advantages of using the HI imagery may be in using it to update initial
411 predictions and to prune ensemble forecasts. This is discussed in section 5.

412 **5 Discussion**

413 Accurate determination of the time of arrival of CMEs at Earth has so far proven
414 difficult. For example, *Millward et al.* [2013] found, with all 3 spacecraft, an average ab-
415 solute error in the arrival time of 7.5 hours when using the CAT to give input values to
416 the WSA-Enlil model. It is worth noting that determining CMEs parameters with CAT-HI
417 is partly subjective due to CMEs not having a well defined edge or geometry. A different
418 user of CAT-HI, such as an experienced forecaster, would get slightly different values for
419 the CME parameters. However, we expect that the overall results would agree with the
420 conclusions of this study (that there are no significant differences between the two tools).
421 Due to the easier availability of data, this study only looked at CMEs from Jan 2016 to
422 Oct 2017 and was considered sufficient for this proof-of-concept study. Any future study
423 should also use data from a wider range of years to reduce the uncertainty in the results
424 and use a more formal testing procedure.

425 The predicted time of arrival of the CME depends on the initial CME parameters
426 such as its speed [*Lee et al.*, 2013; *Mays et al.*, 2015] and the ambient solar wind condi-
427 tions throughout the whole heliosphere [*Lee et al.*, 2015; *Wold et al.*, 2018]. *Möstl et al.*
428 [2014] and *Wold et al.* [2018] have found that on average, the estimated time of arrival is
429 a few hours too early (unlike in Figures 5a and 5b), either because the initial speed of the
430 CME is overestimated or the CME decelerates through the heliosphere. Even for experi-

431 enced forecasters, determining the CME's initial properties is inevitably uncertain. Obser-
432 vational knowledge of the state of the entire solar wind is also not possible to obtain and
433 instead, forecasters must rely on models.

434 In terrestrial weather, ensemble modeling is used to indicate uncertainty in the pre-
435 dictions. Instead of using a single set of initial conditions for one model run, ensemble
436 modeling takes a set of perturbed initial conditions and creates a set of runs (an ensem-
437 ble), which describes the uncertainty in the initial conditions. The spread of the ensem-
438 ble can be used to assign a probability to a particular outcome. Ensemble modeling can
439 be used to improve the forecasting of chaotic systems, such as hurricanes [e.g., *Zhang*
440 *and Krishnamurti*, 1997], and to generate seasonal forecasts [e.g., *Arribas et al.*, 2011;
441 *MacLachlan et al.*, 2015].

442 In recent years, it has become increasingly clear that ensemble modeling could also
443 improve space weather forecasting [*Riley et al.*, 2013; *Henley and Pope*, 2017; *Murray*,
444 2018]. Many studies have been conducted applying ensemble modeling to CME forecast-
445 ing [e.g., *Emmons et al.*, 2013; *Lee et al.*, 2013, 2015; *Cash et al.*, 2015; *Amerstorfer et al.*,
446 2018], including *Mays et al.* [2015] who applied ensemble modeling to an operational sys-
447 tem. *Amerstorfer et al.* [2018] has also applied ensemble modeling to HI observations of
448 CMEs. In general, it has been found that ensemble modeling of CMEs reduces the error
449 in the time of arrival and usually includes the correct prediction in its range. Applying
450 ensemble methods to CME propagation requires consideration of the underlying dynam-
451 ics, as this affects the approach used to set up the ensemble. *Pizzo et al.* [2015] show that
452 CME shock front propagation may be treated more as a deterministic issue (dominated by
453 unknown initial conditions, similar to tsunami propagation), rather than as a chaotic prob-
454 lem (dominated by internal variability, similar to hurricane propagation).

455 CAT-HI gives the opportunity to improve model predictions by two routes: pruning
456 away unlikely ensemble members and providing mid-trajectory corrections, both using the
457 HI data. When an operator makes a prediction using imagery from the LASCO and COR2
458 coronagraphs, they are unable to track the CME after it passes beyond LASCO C3's field
459 of view. With CAT-HI, the STEREO HI data are incorporated into the operational tool,
460 yielding data for a longer period after the Enlil start time (see Figure 4). Therefore, with
461 post-processing of the WSA-Enlil model results to generate synthetic white light images
462 [*Odstrčil and Pizzo*, 2009] it should be possible to compare the original WSA-Enlil runs

463 with the latest HI imagery. The ensemble runs could then be pruned so that the ensemble
464 spread better reflects the true uncertainty, or the model rerun with the new information,
465 providing trajectory corrections for CMEs. This process could be repeated every few
466 hours as new HI data became available, allowing the forecasters to increase the accuracy
467 of their predictions over time, albeit with decreasing forecast lead time. This would be a
468 major step forwards in predicting CME arrival times. It would also be beneficial if the
469 WSA-Enlil model could be rerun with the Enlil inner boundary at a greater distance from
470 the Sun, but currently this is not possible.

471 STEREO-A is in a continuously drifting orbit relative to the Earth and is currently
472 approaching the Earth. As the angle between the Sun-Earth and Sun-STEREO-A lines
473 decreases from -90 degrees towards 0 degrees, the accuracy of determining the CME's
474 initial parameters is expected to worsen. For this study, STEREO-A was located between
475 Earth ecliptic longitudes of -164 and -128 degrees, which is non-ideal. Many authors have
476 recently lobbied for a permanent mission at the L4 or L5 Lagrange points to counter for
477 this loss of capability and to ensure good quality and long term space weather monitoring
478 capabilities [Hapgood, 2017; Wold et al., 2018; Amerstorfer et al., 2018]. CAT-HI
479 could easily be adapted to use imagery from dedicated operational missions at L1 and
480 L4/L5. It would be particularly powerful if a mission at L4/L5 had a heliospheric imager
481 onboard. With the added HI, this would give continuous observation of CMEs from permanent
482 viewing points and improve the quality of space weather monitoring. This study
483 has used science-grade data, as its improved quality allows easier identification of CMEs
484 further out than is possible with beacon-grade data, potentially improving the information
485 available to forecasters. However, while we have shown CAT-HI can use beacon-quality
486 data, we have not investigated performance with this, so cannot state what the benefit is (if
487 any) of science-quality data over beacon-quality. Further work would be required to assess
488 this, and may help to inform downlink requirements for an operational mission.

489 **6 Summary**

490 This paper has introduced an adapted version of the operational CME Analysis Tool,
491 CAT. CAT-HI incorporates Heliospheric Imagery (HI) from the STEREO spacecraft and
492 hence provides the possibility of tracking CMEs out to much greater distances than was
493 possible with CAT. Although the use of HI imagery does not produce an improvement in
494 the initial prediction of a CME's arrival time, it could potentially be used in conjunction

495 with ensemble modelling. Once a WSA-Enlil prediction is made, the model output could
 496 be post-processed to generate synthetic white light imagery. This would allow easy com-
 497 parison with new HI imagery, as this becomes available, allowing the forecast to be up-
 498 dated by pruning ensemble runs. Any new HI imagery could also be used as the basis for
 499 new CME fits to use as input into new model runs, also allowing forecast updates. There-
 500 fore, we see this tool not as an improvement to the CAT tool, but as a proof of concept
 501 for using HI data operationally. This tool also supports the development of a dedicated
 502 L4/L5 operational mission equipped with a heliospheric imager. It is our intention that
 503 CAT-HI will enter use operationally at both NOAA/SWPC and MOSWOC.

04 7 Appendix

05 In this section, we discuss the projection of HI images onto a flat plane, the so-
 06 called "plane of sky". This is used by the coronagraphs, and it is helpful to apply the
 07 same concept to the HI images, so they can be treated equivalently by CAT-HI. Figure 6
 08 shows the viewing geometry of the HI imagers. In CAT-HI, it has been assumed that the
 09 image can be displayed as a flat, square image like COR2, which is the red plane in Fig-
 10 ure6. However, the HIs have wide fields of view. Therefore, the correct projection is onto
 11 the inside of a sphere, which is the blue plane in Figure 6. This curved image then needs
 12 transforming to the plane of sky. In this appendix, we quantify the difference in radial
 13 distances under these two projections in order to understand whether a flat projection is
 14 justified.

20 In Figure 6, position O represents the location of STEREO A (or B). S represents
 the position of the Sun, which for convenience, lies in both the red and blue planes. OA
 522 (or OV) is the viewing direction of a HI camera and OC (or OF) is the direction of the
 523 point of interest in the image, the leading edge of the CME. α_c and β_c are the horizontal
 524 and vertical angles between the viewing direction and the CME direction. α is the angle
 525 between the viewing direction and the Sun, which from *Eyles et al.* [2009] is 14° for HI-1
 526 and 53.7° for HI-2.

527 We can use Figure 6 to calculate the distance CS , the "correct" plane of sky pro-
 528 jection. This can then be compared to the original determination where the HI image
 529 was projected as a flat square. We call the distance $OS = R_S$, the Sun-spacecraft dis-
 530 tance. Then $OA = R_S \cos(\alpha)$ and $AS = R_S \sin(\alpha)$. $AB = R_S \cos(\alpha) \tan(\alpha_c)$ so $BS =$

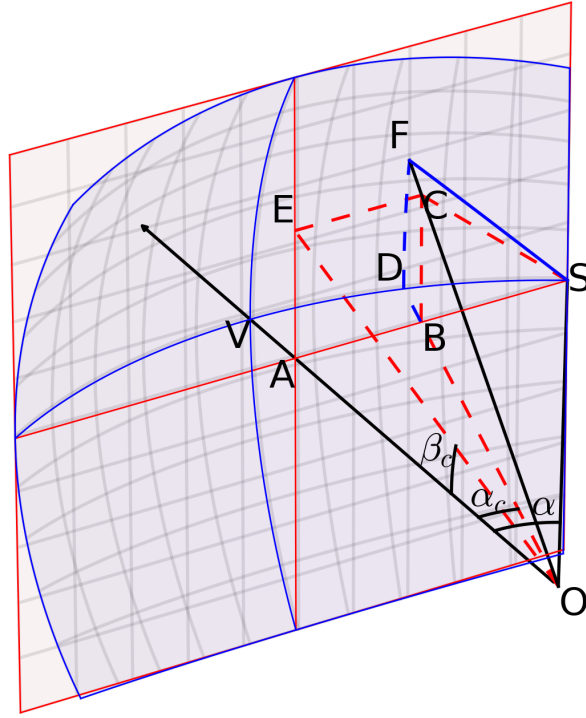


Figure 6. The projection of HI images onto a flat plane (red) and the inside of a sphere (blue). O is the location of STEREO A and S is the location of the Sun. OA/OV is the viewing direction of the HI camera. OC/OF is the direction of the point of interest, the leading edge of the CME. α_c and β_c are the horizontal and vertical angles from the viewing direction to the CME. α is the angle between the viewing direction and the Sun.

$R_S(\sin(\alpha) - \cos(\alpha) \tan(\alpha_c))$. $AE = R_S \cos(\alpha) \tan(\beta_c)$ and $AE = BC$. Finally, we can get CS_{Circ} using Pythagoras' theorem (equation (2)), where the subscript *circ* is to distinguish that this difference refers to the correct projection.

$$CS_{Circ} = R_S \sqrt{\cos^2(\alpha) \tan^2(\beta_c) + (\sin(\alpha) - \cos(\alpha) \tan(\alpha_c))^2} \quad (2)$$

To compare to CAT-HI, we get the equivalent distance in the coordinates of the flat projection, where the x -coordinate is in the α direction and the y -coordinate is in the β direction. The equivalent radial distance CS_{Flat} is given by equation (3).

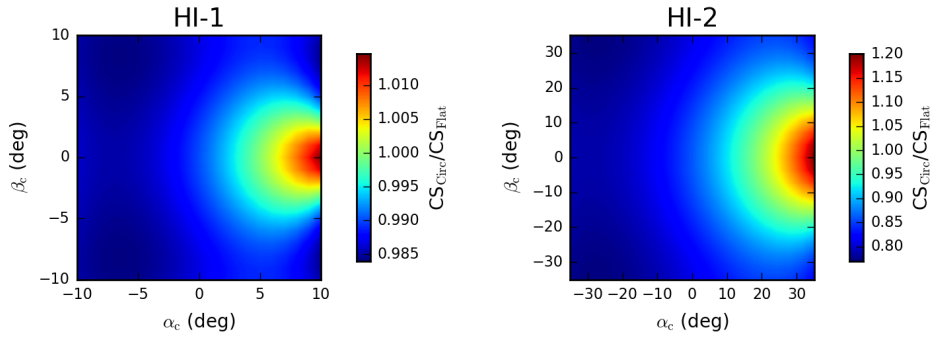


Figure 7. CS_{Circ}/CS_{Flat} for all values of angles α_c and β_c . Left shows HI-1 and right shows HI-2. The sun is to the right in these subfigures.

$$CS_{Flat} = R_S \sqrt{(\alpha - \alpha_c)^2 + \beta_c^2} \quad (3)$$

We now calculate CS_{Circ}/CS_{Flat} for all combinations of α_c and β_c possible in the HI-1 and HI-2 viewing geometries. This is shown in Figure 7. Note that the scales are different for the HI-1 and HI-2 cases.

For HI-1, we can see that the greatest difference between CS_{Circ} and CS_{Flat} is $\sim 1.5\%$, or 1.015 on the colourbar in Figure 7 (left). Typical radial distances of the leading edge of the CME might be of the order 30-50 solar radii (see Figure 4, giving a maximum possible error of less than a solar radii. Given the other assumptions and constraints of CAT-HI, this difference is not significant.

For HI-2, the greatest difference is $\sim 22\%$, or 1.22 on the colourbar in Figure 7 (right). If CAT-HI measures a point at 150 solar radii in the plane of the sky with the flat field assumption, it will overestimate the distance by ~ 27 solar radii, a significant distance. Hence, assuming that the HI-2 image can be treated as a flat square is a poor assumption and will lead to significant errors when matching the lemniscate to the image. This does not affect the results presented in this paper, as we have not included any matches from HI-2.

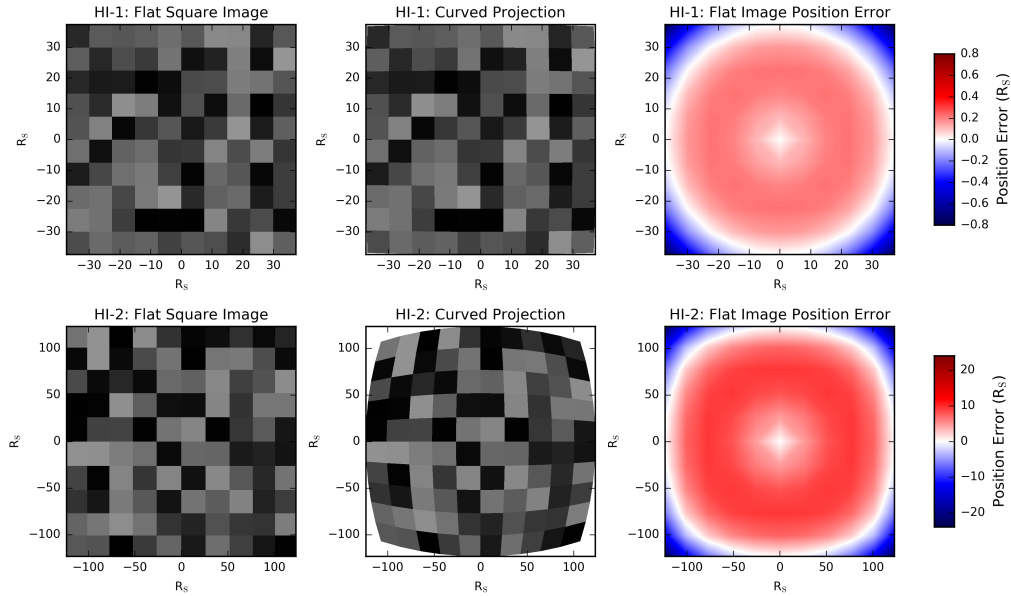


Figure 8. Flat vs. Curved Projections. Top row is HI-1, bottom row is HI-2. Left column shows an image plotted as a square and the middle column shows the image plotted onto the inside of a sphere. The right column shows the location error for each point in the image when projected as a flat square. The pointing direction is general and assumes a Sun-Spacecraft distance of 215 solar radii.

We can also observe the distortion by comparing the flat, square assumption with the equivalent image projected onto the inside of a sphere. This is illustrated with "fake" images in Figure 8. The top row shows HI-1 projections and the bottom row shows HI-2 projections. The left column shows the image plotted as a flat square whilst the middle column shows the image plotted onto the inside of a sphere, as it would appear looking along the viewing direction of the telescope. The Sun-Spacecraft distance is set at 215 solar radii, and is not assumed to point in a particular direction. The right column shows the position error of any point in the image when projected as a flat square. So in order for the flat image to match the curved image, those pixels that are red need moving radially outwards by this amount. Likewise, blue pixels need moving radially inwards to match the curved image.

Figure 7 shows us that for HI-1, there is very little difference between the correct curved projection (in the middle) and the flat projection (on the left). The right column shows us that assuming a Sun-Spacecraft distance of 215 solar radii, features in the flat projection will be located no more than 0.8 solar radii away from the correct position (in

a plane containing the Sun). However, for HI-2, the wider field of view creates a much greater distortion, and towards the corners, the leading edge of the CME can be projected in the wrong place by over 20 solar radii. This is a more significant error.

This analysis shows us that the curvature of the image makes a negligible difference for the HI-1 images, and so we have used the more convenient flat square projection in CAT-HI. However, the error that comes from this assumption for HI-2 is much greater. For this study, we did not use HI-2 images, so the results are not affected, but these effects should be considered for future studies if it is desired to extend these effects further out.

Acknowledgments

S.J.W. was supported by NERC Studentship NE/L002493/1. S.J.W. would also like to acknowledge the industrial placement grant provided by the Central England NERC Training Alliance (CENTA) that enabled the work to be undertaken at the Met Office.

Imagery for SOHO and STEREO can be found at the UK Solar System Data Centre: <https://www.ukssdc.ac.uk/solar/>. DSCOVR data can be found at: <https://www.ngdc.noaa.gov/dscovr/portal/#/>.

We would also like to thank V. Pizzo and two anonymous reviewers for their very helpful suggestions in revising this paper.

References

- Amerstorfer, T., C. Möstl, P. Hess, M. Temmer, M. L. Mays, M. A. Reiss, P. Lowrance, and P.-A. Bourdin (2018), Ensemble Prediction of a Halo Coronal Mass Ejection Using Heliospheric Imagers, *Space Weather*, *16*(7), 784–801, doi:10.1029/2017SW001786.
- Arge, C., J. Luhmann, D. Odstrčil, C. Schrijver, and Y. Li (2004), Stream structure and coronal sources of the solar wind during the May 12th, 1997 CME, *Journal of Atmospheric and Solar-Terrestrial Physics*, *66*(15), 1295 – 1309, doi:<https://doi.org/10.1016/j.jastp.2004.03.018>, towards an Integrated Model of the Space Weather System.
- Arge, C. N., and V. J. Pizzo (2000), Improvement in the prediction of solar wind conditions using near-real time solar magnetic field updates, *J Geophys Res - Space*, *105*(A5), 10,465–10,479, doi:10.1029/1999JA000262.
- Arge, C. N., D. Odstrčil, V. J. Pizzo, and L. R. Mayer (2003), Improved Method for Specifying Solar Wind Speed Near the Sun, *AIP Conference Proceedings*, *679*(1), 190–193,

doi:10.1063/1.1618574.

- Arribas, A., M. Glover, A. Maidens, K. Peterson, M. Gordon, C. MacLachlan, R. Graham, D. Fereday, J. Camp, A. A. Scaife, P. Xavier, P. McLean, A. Colman, and S. Cusack (2011), The GloSea4 Ensemble Prediction System for Seasonal Forecasting, *Mon. Wea. Rev.*, *139*(6), 1891–1910, doi:10.1175/2010MWR3615.1.
- Barnard, L. A., C. A. Koning, C. J. Scott, M. J. Owens, J. Wilkinson, and J. A. Davies (2017), Testing the current paradigm for space weather prediction with heliospheric imagers, *Space Weather*, *15*(6), 782–803, doi:10.1002/2017SW001609.
- Brueckner, G. E., R. A. Howard, M. J. Koomen, C. M. Korendyke, D. J. Michels, J. D. Moses, D. G. Socker, K. P. Dere, P. L. Lamy, A. Llebaria, M. V. Bout, R. Schwenn, G. M. Simnett, D. K. Bedford, and C. J. Eyles (1995), The Large Angle Spectroscopic Coronagraph (LASCO), *Solar Physics*, *162*(1), 357–402, doi:10.1007/BF00733434.
- Cash, M. D., D. A. Biesecker, V. Pizzo, C. A. Koning, G. Millward, C. N. Arge, C. J. Henney, and D. Odstrčil (2015), Ensemble modeling of the 23 July 2012 coronal mass ejection, *Space Weather*, *13*(10), 611–625, doi:10.1002/2015SW001232.
- Colaninno, R. C., A. Vourlidas, and C. C. Wu (2013), Quantitative comparison of methods for predicting the arrival of coronal mass ejections at earth based on multiview imaging, *Journal of Geophysical Research: Space Physics*, *118*(11), 6866–6879, doi:10.1002/2013JA019205.
- de Koning, C. A., G. Millward, V. J. Pizzo, and D. A. Biesecker (2012), Problems encountered when characterizing cmes in an operational setting, in *Space Weather: The Space Radiation Environment*, edited by Q. Hu, G. Li, G. P. Zank, G. Fry, X. Ao, and J. Adams, Proc. 11th Ann. Intl. Astrophys Conf., AIP, Palm Springs, CA.
- Domingo, V., B. Fleck, and A. I. Poland (1995), The SOHO mission: An overview, *Solar Physics*, *162*(1), 1–37, doi:10.1007/BF00733425.
- Driesman, A., S. Hynes, and G. Cancro (2008), The STEREO Observatory, *Space Science Reviews*, *136*(1), 17–44, doi:10.1007/s11214-007-9286-z.
- Emmons, D., A. Acebal, A. Pulkkinen, A. Taktakishvili, P. MacNeice, and D. Odstrčil (2013), Ensemble forecasting of coronal mass ejections using the WSA-ENLIL with CONED Model, *Space Weather*, *11*(3), 95–106, doi:10.1002/swe.20019.
- Eyles, C. J., R. A. Harrison, C. J. Davis, N. R. Waltham, B. M. Shaughnessy, H. C. A. Mapson-Menard, D. Bewsher, S. R. Crothers, J. A. Davies, G. M. Simnett, R. A. Howard, J. D. Moses, J. S. Newmark, D. G. Socker, J.-P. Halain, J.-M. Defise, E. Mazy,

- 636 and P. Rochus (2009), The Heliospheric Imagers Onboard the STEREO Mission, *Solar*
637 *Physics*, 254(2), 387–445, doi:10.1007/s11207-008-9299-0.
- 38 Hapgood, M. (2017), L1L5Together: Report of Workshop on Future Missions to Moni-
639 tor Space Weather on the Sun and in the Solar Wind Using Both the L1 and L5 La-
40 grange Points as Valuable Viewpoints, *Space Weather*, 15(5), 654–657, doi:10.1002/
641 2017SW001652.
- 642 Harrison, R. A., J. A. Davies, D. Biesecker, and M. Gibbs (2017), The application of he-
43 liospheric imaging to space weather operations: Lessons learned from published studies,
644 *Space Weather*, 15(8), 985–1003, doi:10.1002/2017SW001633.
- 645 Henley, E. M., and E. C. D. Pope (2017), Cost-Loss Analysis of Ensemble Solar Wind
646 Forecasting: Space Weather Use of Terrestrial Weather Tools, *Space Weather*, 15(12),
647 1562–1566, doi:10.1002/2017SW001758.
- 48 Hill, F. (2018), The Global Oscillation Network Group Facility - An Example of Research
649 to Operations in Space Weather, *Space Weather*, 0(0), doi:10.1029/2018SW002001.
- 50 Howard, R. A., J. D. Moses, A. Vourlidis, J. S. Newmark, D. G. Socker, S. P. Plun-
651 kett, C. M. Korendyke, J. W. Cook, A. Hurley, J. M. Davila, W. T. Thompson, O. C.
52 St Cyr, E. Mentzell, K. Mehalick, J. R. Lemen, J. P. Wuelser, D. W. Duncan, T. D.
53 Tarbell, C. J. Wolfson, A. Moore, R. A. Harrison, N. R. Waltham, J. Lang, C. J.
654 Davis, C. J. Eyles, H. Mapson-Menard, G. M. Simnett, J. P. Halain, J. M. Defise,
55 E. Mazy, P. Rochus, R. Mercier, M. F. Ravet, F. Delmotte, F. Auchere, J. P. De-
656 laboudiniere, V. Bothmer, W. Deutsch, D. Wang, N. Rich, S. Cooper, V. Stephens,
657 G. Maahs, R. Baugh, D. McMullin, and T. Carter (2008), Sun Earth Connection Coro-
58 nal and Heliospheric Investigation (SECCHI), *Space Science Reviews*, 136(1), 67, doi:
10.1007/s11214-008-9341-4.
- 660 Howard, T. A., and S. J. Tappin (2010), Application of a new phenomenological coronal
661 mass ejection model to space weather forecasting, *Space Weather*, 8(7), doi:10.1029/
662 2009SW000531.
- 663 Kaiser, M. L., T. A. Kucera, J. M. Davila, O. C. St. Cyr, M. Guhathakurta, and E. Chris-
664 tian (2008), The STEREO Mission: An Introduction, *Space Science Reviews*, 136(1),
665 5–16, doi:10.1007/s11214-007-9277-0.
- 666 Lee, C. O., C. N. Arge, D. Odstrčil, G. Millward, V. Pizzo, J. M. Quinn, and C. J. Henney
667 (2013), Ensemble Modeling of CME Propagation, *Solar Physics*, 285(1), 349–368, doi:
668 10.1007/s11207-012-9980-1.

- 669 Lee, C. O., C. N. Arge, D. Odstrčil, G. Millward, V. Pizzo, and N. Lugaz (2015), Ensemble
670 Modeling of Successive Halo CMEs: A Case Study, *Solar Physics*, 290(4), 1207–
671 1229, doi:10.1007/s11207-015-0667-2.
- 672 Lugaz, N. (2010), Accuracy and Limitations of Fitting and Stereoscopic Methods to Deter-
673 mine the Direction of Coronal Mass Ejections from Heliospheric Imagers Observations,
674 *Solar Physics*, 267(2), 411–429, doi:10.1007/s11207-010-9654-9.
- 675 Lugaz, N., P. Kintner, C. Möstl, L. K. Jian, C. J. Davis, and C. J. Farrugia (2012), He-
676 liospheric Observations of STEREO-Directed Coronal Mass Ejections in 2008 - 2010:
677 Lessons for Future Observations of Earth-Directed CMEs, *Solar Physics*, 279(2), 497–
678 515, doi:10.1007/s11207-012-0007-8.
- 679 MacLachlan, C., A. Arribas, K. A. Peterson, A. Maidens, D. Fereday, A. A. Scaife,
680 M. Gordon, M. Vellinga, A. Williams, R. E. Comer, J. Camp, P. Xavier, and G. Madec
681 (2015), Global Seasonal forecast system version 5 (GloSea5): a high-resolution seasonal
682 forecast system, *Q. J. R. Met Soc*, 141(689), 1072–1084, doi:10.1002/qj.2396.
- 683 Mays, M. L., A. Taktakishvili, A. Pulkkinen, P. J. MacNeice, L. Rastätter, D. Odstrčil,
684 L. K. Jian, I. G. Richardson, J. A. LaSota, Y. Zheng, and M. M. Kuznetsova (2015),
685 Ensemble Modeling of CMEs Using the WSA–ENLIL+Cone Model, *Solar Physics*,
686 290(6), 1775–1814, doi:10.1007/s11207-015-0692-1.
- 687 Millward, G., D. Biesecker, V. Pizzo, and C. A. Koning (2013), An operational software
688 tool for the analysis of coronagraph images: Determining CME parameters for input
689 into the WSA-Enlil heliospheric model, *Space Weather*, 11(2), 57–68, doi:10.1002/swe.
690 20024.
- 691 Möstl, C., K. Amla, J. R. Hall, P. C. Liewer, E. M. D. Jong, R. C. Colaninno, A. M.
692 Veronig, T. Rollett, M. Temmer, V. Peinhart, J. A. Davies, N. Lugaz, Y. D. Liu, C. J.
693 Farrugia, J. G. Luhmann, B. Vršnak, R. A. Harrison, and A. B. Galvin (2014), Connect-
694 ing Speeds, Directions and Arrival Times of 22 Coronal Mass Ejections from the Sun
695 to 1 AU, *Astrophys J*, 787(2), 119, doi:10.1088/0004-637X/787/2/119.
- 696 Murray, S. A. (2018), The importance of ensemble techniques for operational space
697 weather forecasting, *Space Weather*, 16(7), 777–783, doi:10.1029/2018SW001861.
- 698 Odstrčil, D. (2003), Modeling 3-D solar wind structure, *Adv Space Res*, 32(4), 497 – 506,
699 doi:https://doi.org/10.1016/S0273-1177(03)00332-6.
- 700 Odstrčil, D., and V. J. Pizzo (1999), Distortion of the interplanetary magnetic field by
701 three-dimensional propagation of coronal mass ejections in a structured solar wind,

702 *Journal of Geophysical Research: Space Physics*, 104(A12), 28,225–28,239, doi:
703 10.1029/1999JA900319.

704 Odstrčil, D., and V. J. Pizzo (2009), Numerical Heliospheric Simulations as Assisting Tool
705 for Interpretation of Observations by STEREO Heliospheric Imagers, *Solar Physics*,
706 259(1), 297–309, doi:10.1007/s11207-009-9449-z.

707 Odstrčil, D., J. A. Linker, R. Lionello, Z. Mikic, P. Riley, V. J. Pizzo, and J. G. Luhmann
708 (2002), Merging of coronal and heliospheric numerical two-dimensional MHD models,
709 *Journal of Geophysical Research: Space Physics*, 107(A12), SSH 14–1–SSH 14–11, doi:
710 10.1029/2002JA009334.

711 Parsons, A., D. Biesecker, D. Odstrčil, G. Millward, S. Hill, and V. Pizzo (2011), Wang-
712 Sheeley-Arge-Enlil Cone Model Transitions to Operations, *Space Weather*, 9(3), doi:
713 10.1029/2011SW000663.

714 Pizzo, V. J., C. Koning, M. Cash, G. Millward, D. A. Biesecker, L. Puga, M. Codrescu,
715 and D. Odstrčil (2015), Theoretical basis for operational ensemble forecasting of coro-
716 nal mass ejections, *Space Weather*, 13(10), 676–697, doi:10.1002/2015SW001221.

717 Pulkkinen, A., E. Bernabeu, A. Thomson, A. Viljanen, R. Pirjola, D. Boteler, J. Eichner,
718 P. J. Cilliers, D. Welling, N. P. Savani, R. S. Weigel, J. J. Love, C. Balch, C. M. Ng-
719 wira, G. Crowley, A. Schultz, R. Kataoka, B. Anderson, D. Fugate, J. J. Simpson, and
720 M. MacAlester (2017), Geomagnetically induced currents: Science, engineering, and
721 applications readiness, *Space Weather*, 15(7), 828–856, doi:10.1002/2016SW001501.

722 Redmon, R. J., D. B. Seaton, R. Steenburgh, J. He, and J. V. Rodriguez (2018), September
723 2017's Geoeffective Space Weather and Impacts to Caribbean Radio Communications
724 during Hurricane Response, *Space Weather*, 0(ja), doi:10.1029/2018SW001897.

725 Riley, P., J. A. Linker, and Z. Mikic (2013), On the application of ensemble modeling
726 techniques to improve ambient solar wind models, *J Geophys Res - Space*, 118(2), 600–
727 607, doi:10.1002/jgra.50156.

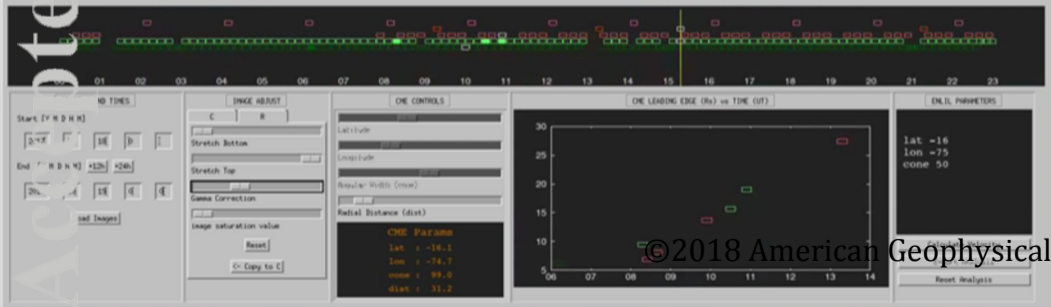
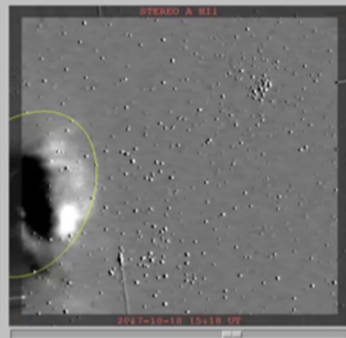
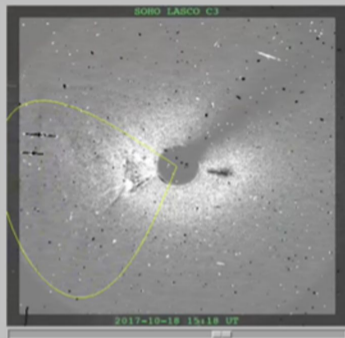
728 Rouillard, A. P., J. A. Davies, R. J. Forsyth, A. Rees, C. J. Davis, R. A. Harrison,
729 M. Lockwood, D. Bewsher, S. R. Crothers, C. J. Eyles, M. Hapgood, and C. H. Perry
730 (2008), First imaging of corotating interaction regions using the STEREO spacecraft,
731 *Geophysical Research Letters*, 35(10), doi:10.1029/2008GL033767.

732 Sheeley Jr., N. R. (2017), Origin of the Wang–Sheeley–Arge solar wind model, *History of*
733 *Geo- and Space Sciences*, 8(1), 21–28, doi:10.5194/hgss-8-21-2017.

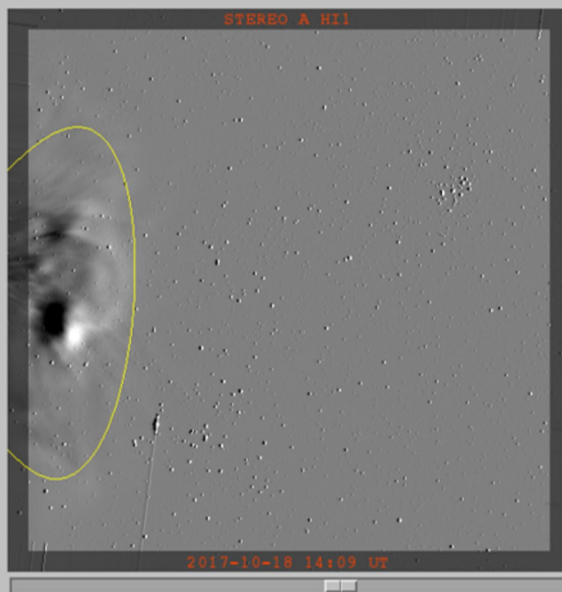
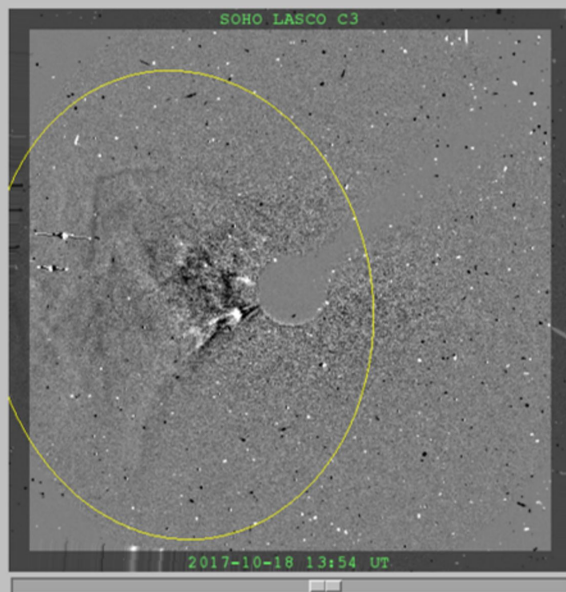
- 734 Sibley, A., D. Biesecker, G. Millward, and M. Gibbs (2012), Space weather, impacts and
735 forecasting: an overview, *Weather*, 67(5), 115–120, doi:10.1002/wea.1915.
- 736 Wang, Y.-M., and N. R. Sheeley, Jr. (1990), Solar wind speed and coronal flux-tube ex-
737 pansion, *apj*, 355, 726–732, doi:10.1086/168805.
- 738 Wold, A. M., M. L. Mays, A. Taktakishvili, L. K. Jian, D. Odstrčil, and P. MacNeice
739 (2018), Verification of real-time WSA-ENLIL+Cone simulations of CME arrival-
740 time at the CCMC from 2010 to 2016, *J. Space Weather Space Clim.*, 8, A17, doi:
741 10.1051/swsc/2018005.
- 742 Xie, H., L. Ofman, and G. Lawrence (2004), Cone model for halo CMEs: Application to
743 space weather forecasting, *J Geophys Res - Space*, 109(A3), doi:10.1029/2003JA010226.
- 744 Zhang, Z., and T. N. Krishnamurti (1997), Ensemble Forecasting of Hurricane Tracks,
745 *Bull. Amer Meteor Soc*, 78(12), 2785–2796, doi:10.1175/1520-0477(1997)078<2785:
746 EFOHT>2.0.CO;2.

Figure 1.

Accepted Article



Accepted Article



ID TIMES

Start [Y M D H M]

2017 10 13 12 30

End [Y M D H M] +12h +24h

2017 10 13 12 30

Load Images

IMAGE ADJUST

C R

Stretch Bottom

Stretch Top

Gamma Correction

image saturation value

Reset

Copy to R ->

CME CONTROLS

Latitude

Longitude

Angular Width (cone)

Radial Distance (dist)

CME Params

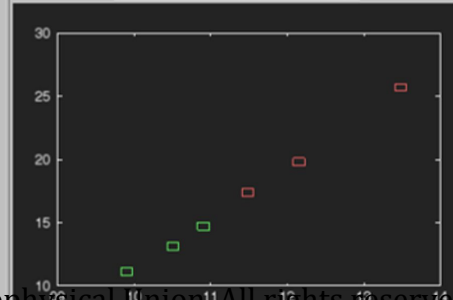
lat : -4.4

lon : -36.5

cone : 58

dist : 28.7

CME LEADING EDGE (R_s) vs TIME (UT)



ENLIL PARAMETERS

T 2017-10-18 12:30

lat -4

lon -37

cone 58

Vel 794

Calculate Velocity

Export Analysis

Reset Analysis

Accepted Article

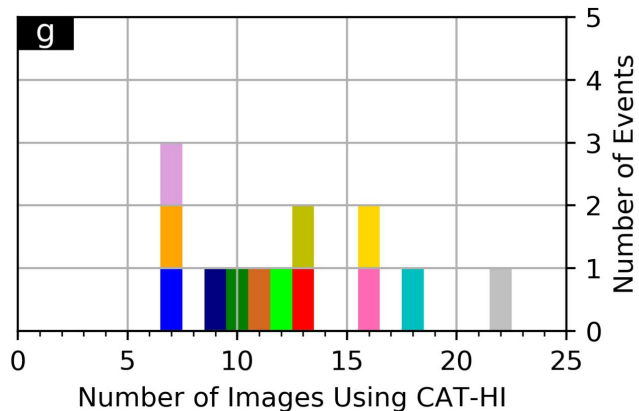
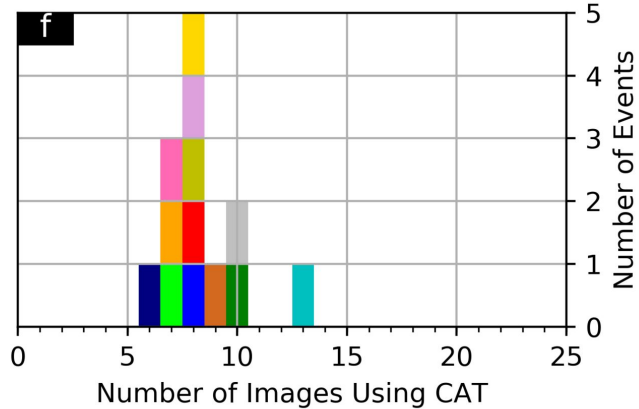
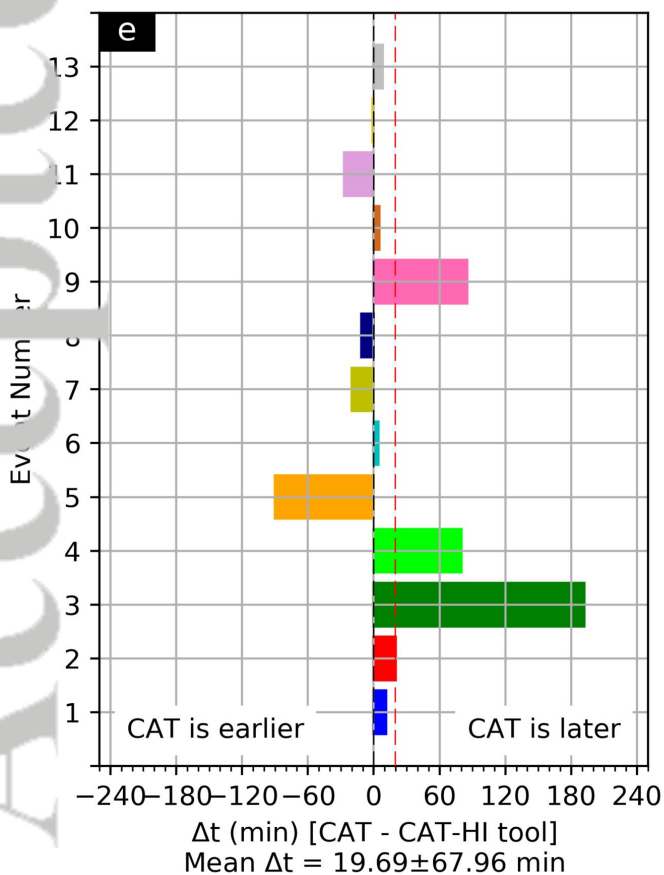
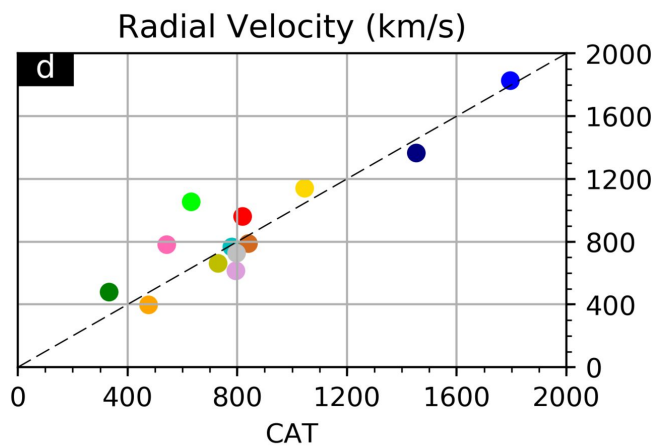
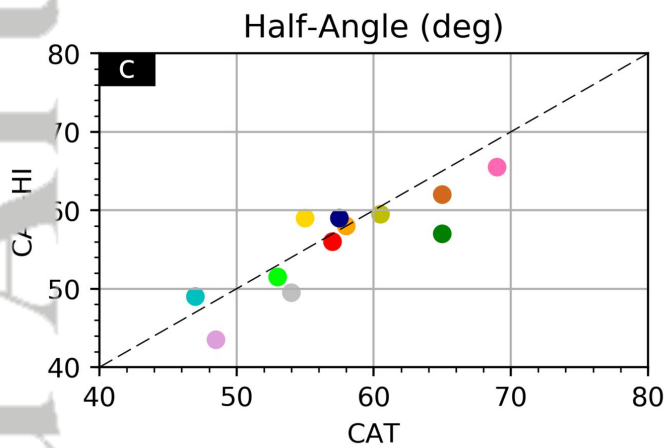
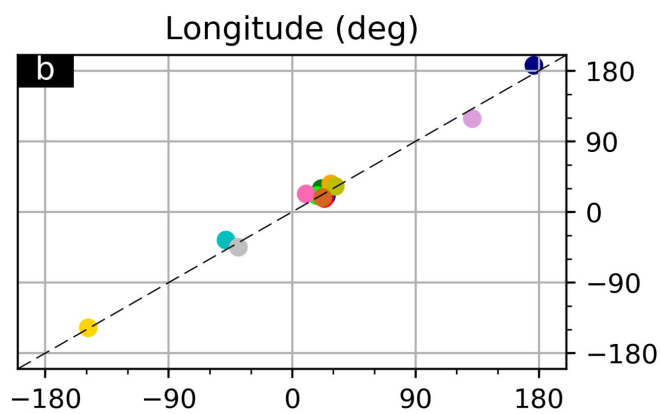
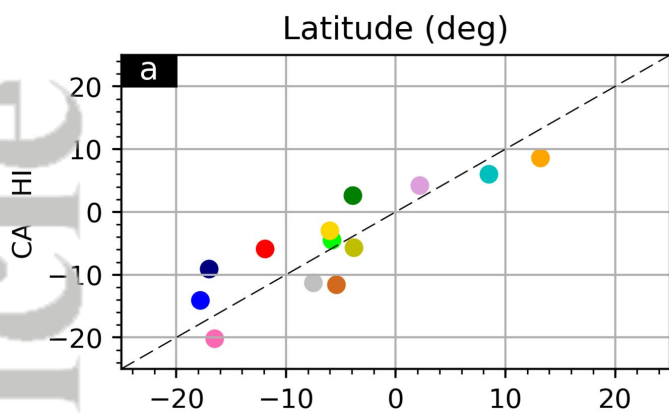
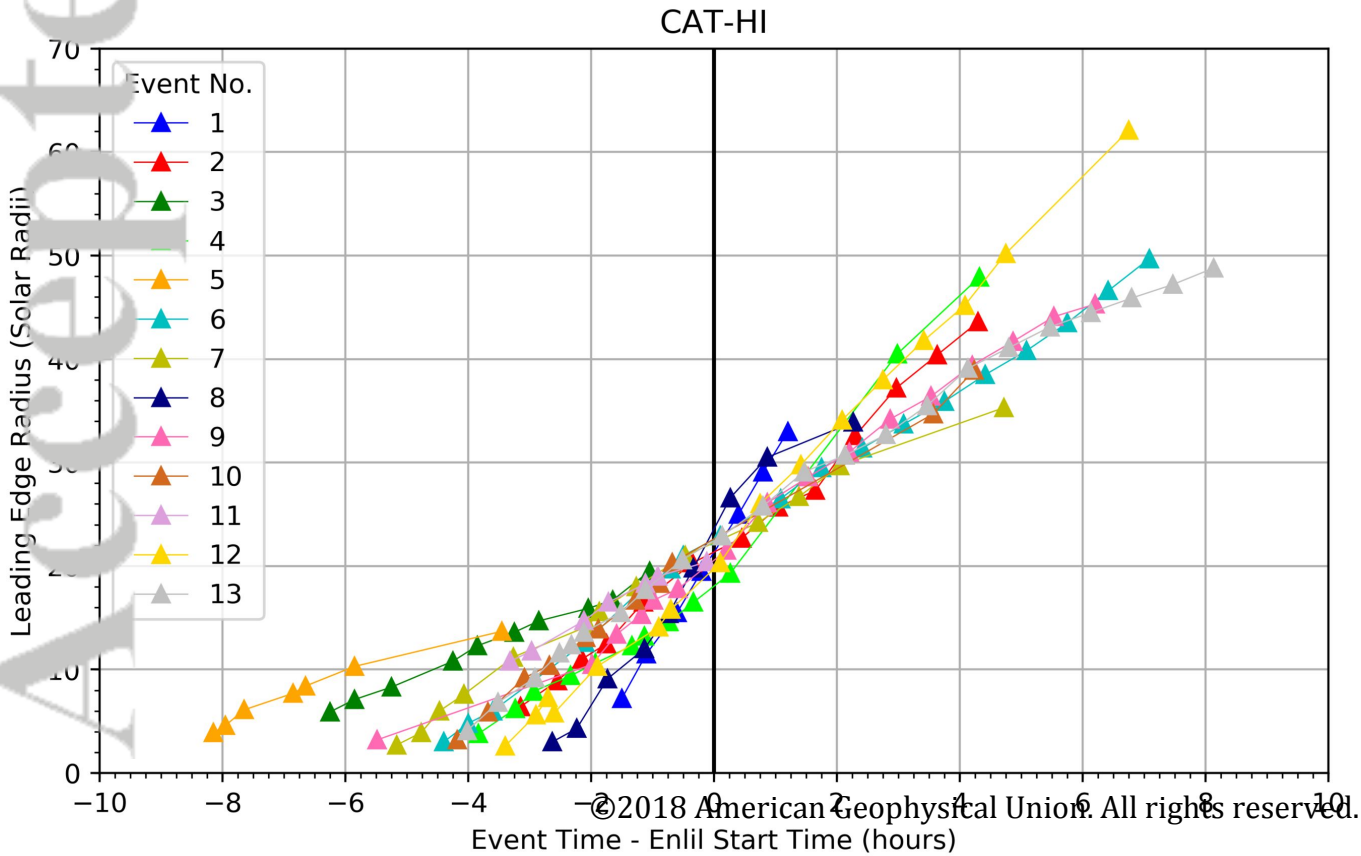
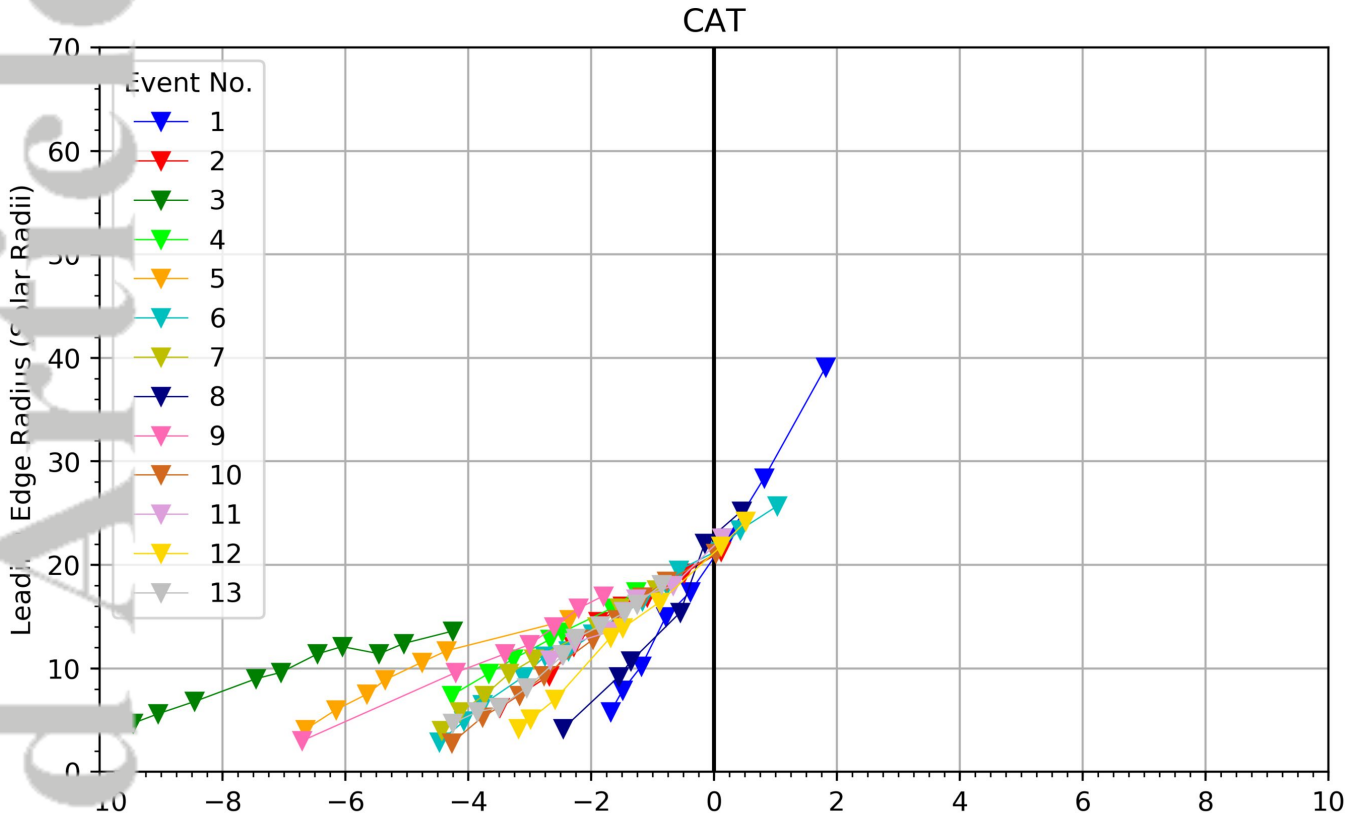


Figure 4.

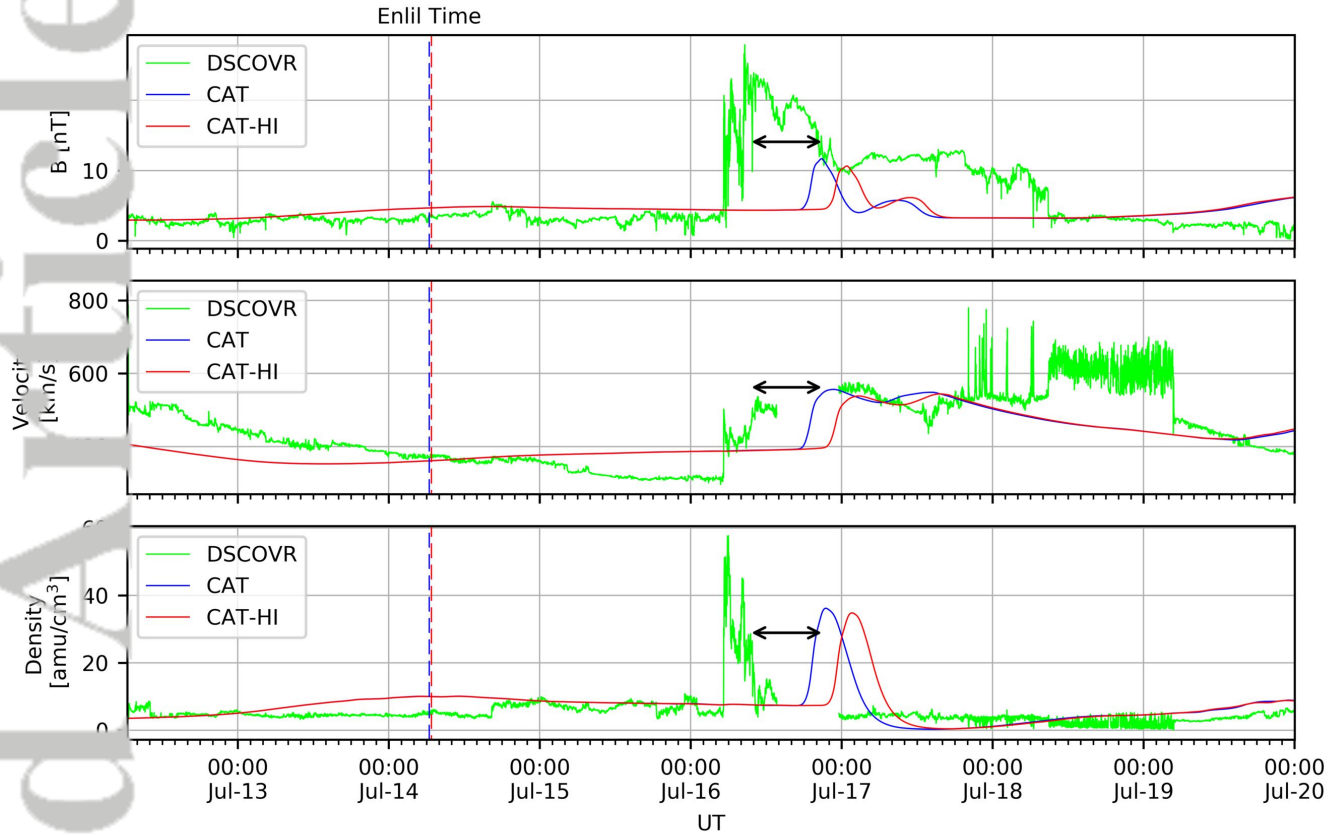
Accepted Article

Leading edge of CME vs. Time



Accepted Article

(a) Date of CME: 2017-07-14



(b) Date of CMEs: 2017-09-05 2017-09-06

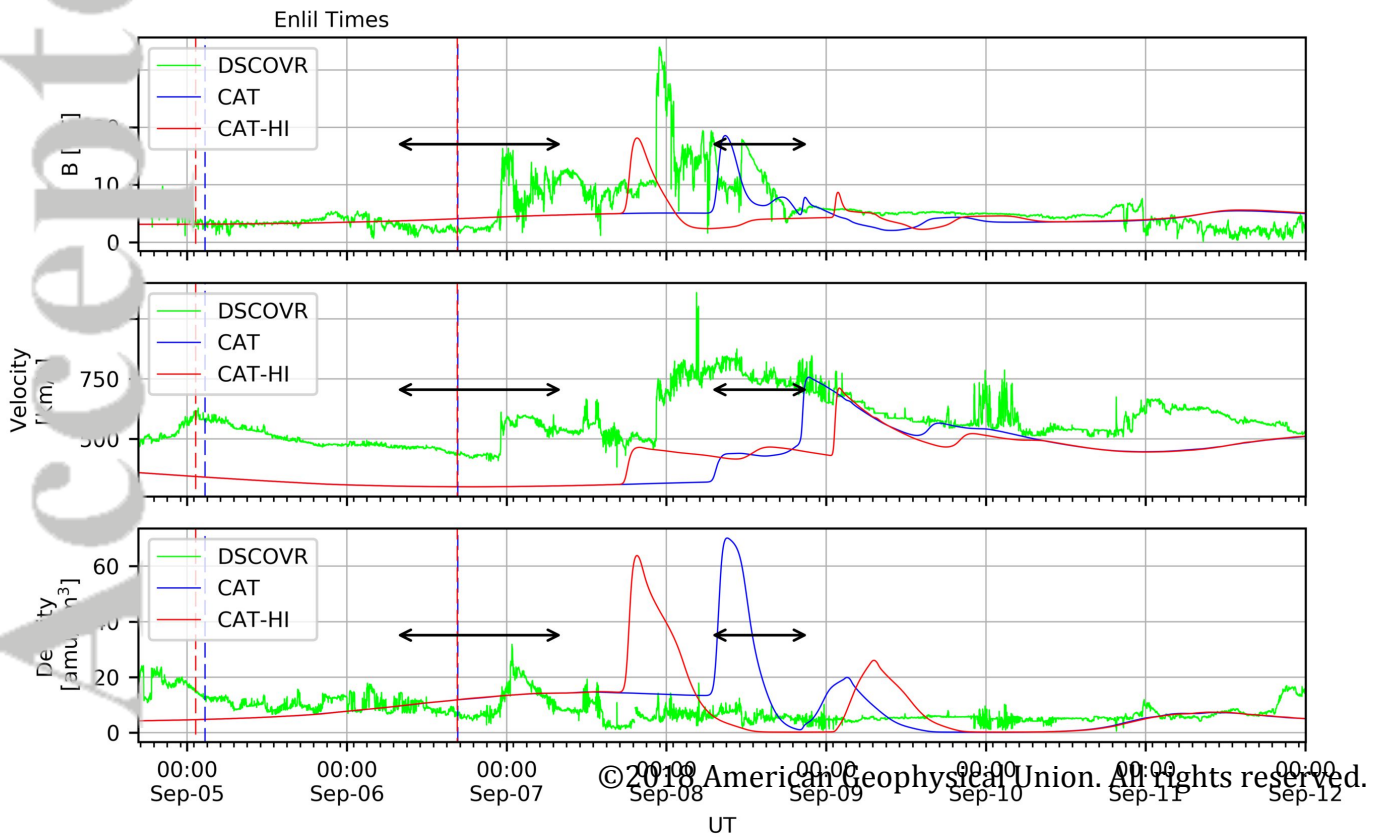
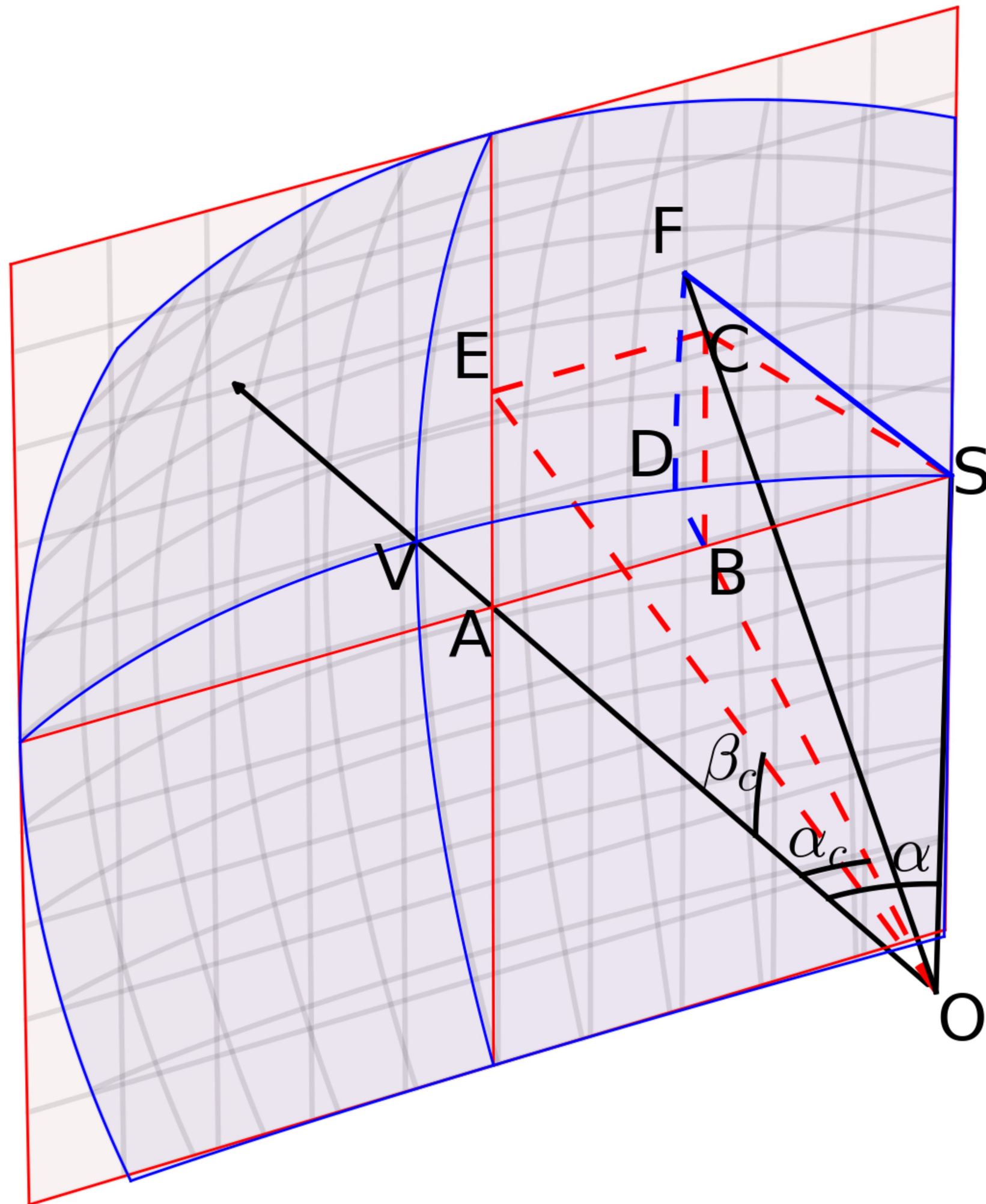
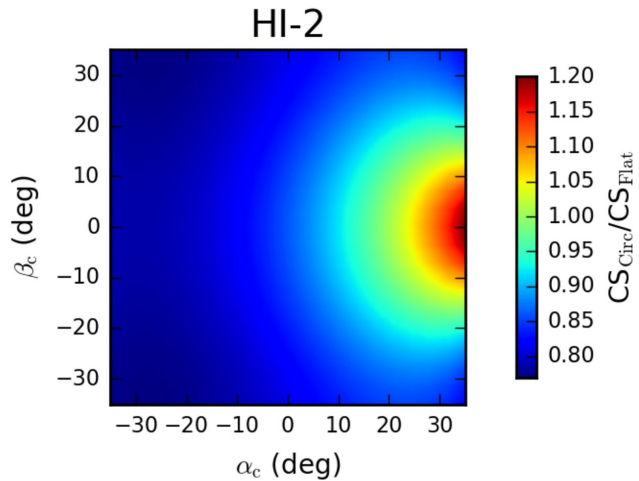
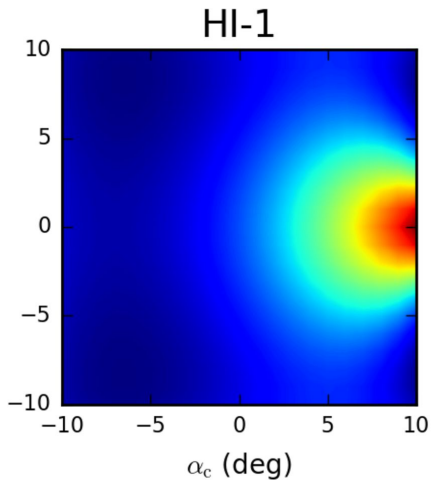


Figure 6.

Accepted Article

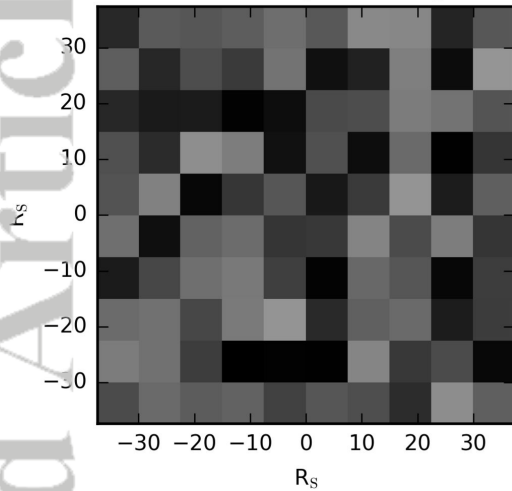


Accepted Article

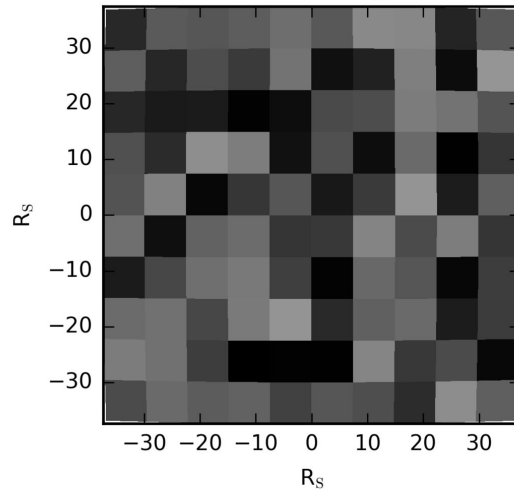


Accepted Article

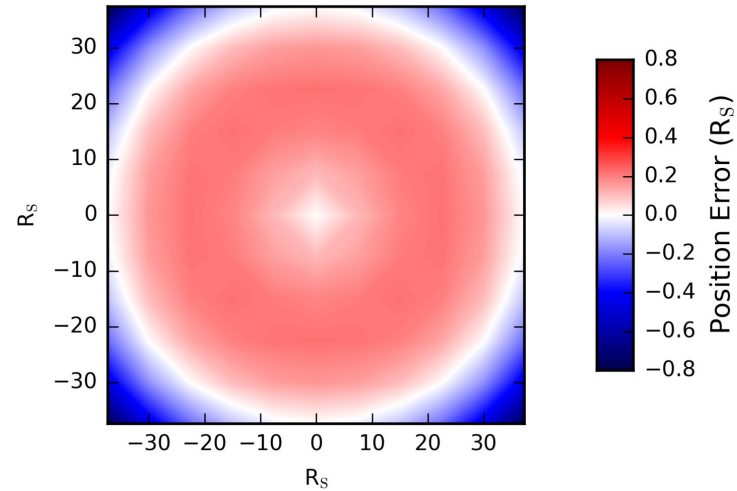
HI-1: Flat Square Image



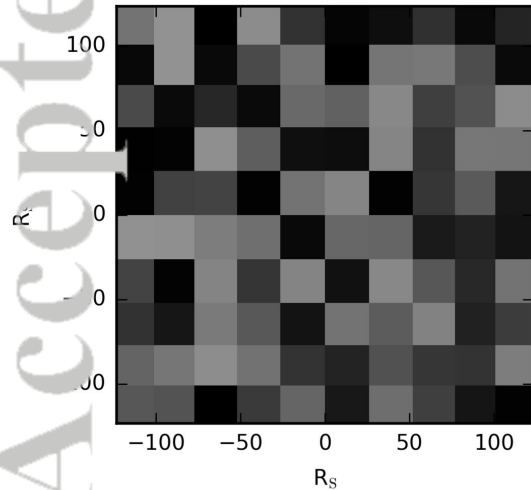
HI-1: Curved Projection



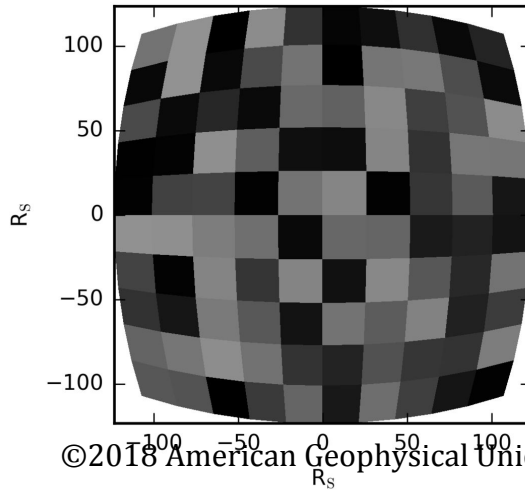
HI-1: Flat Image Position Error



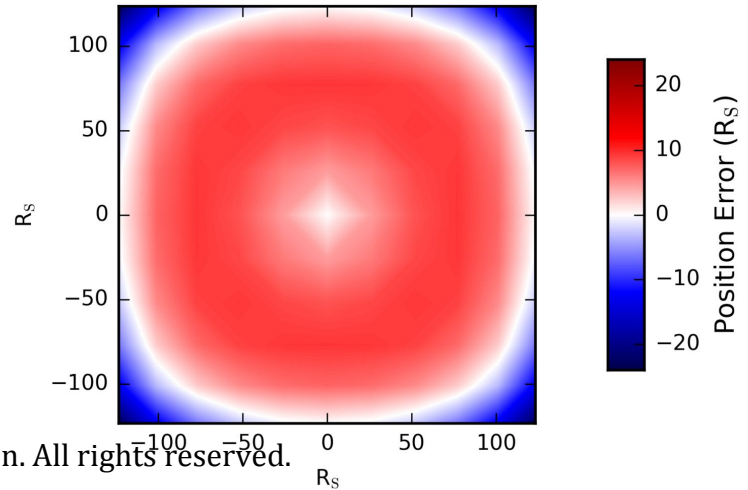
HI-2: Flat Square Image

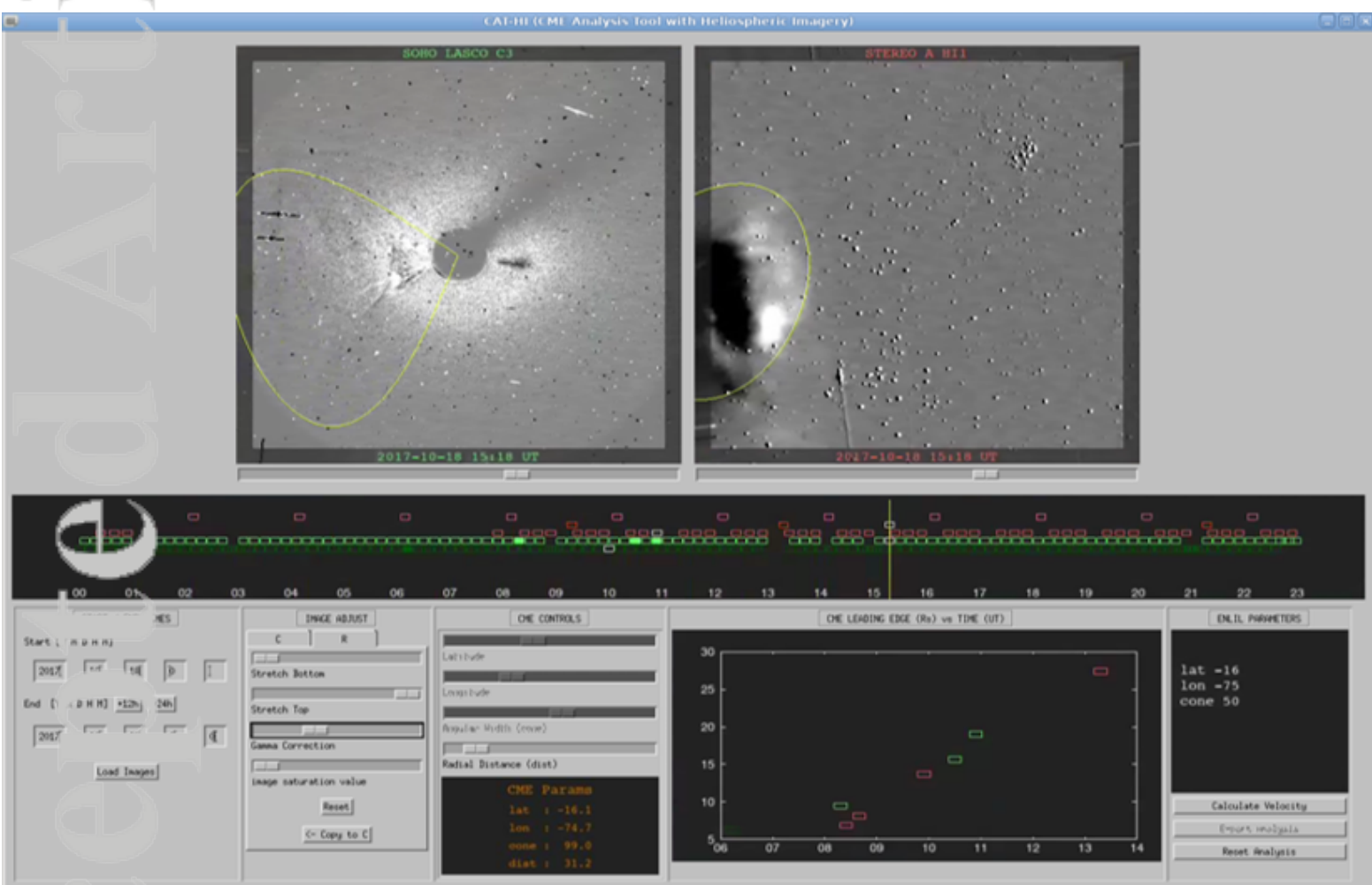


HI-2: Curved Projection

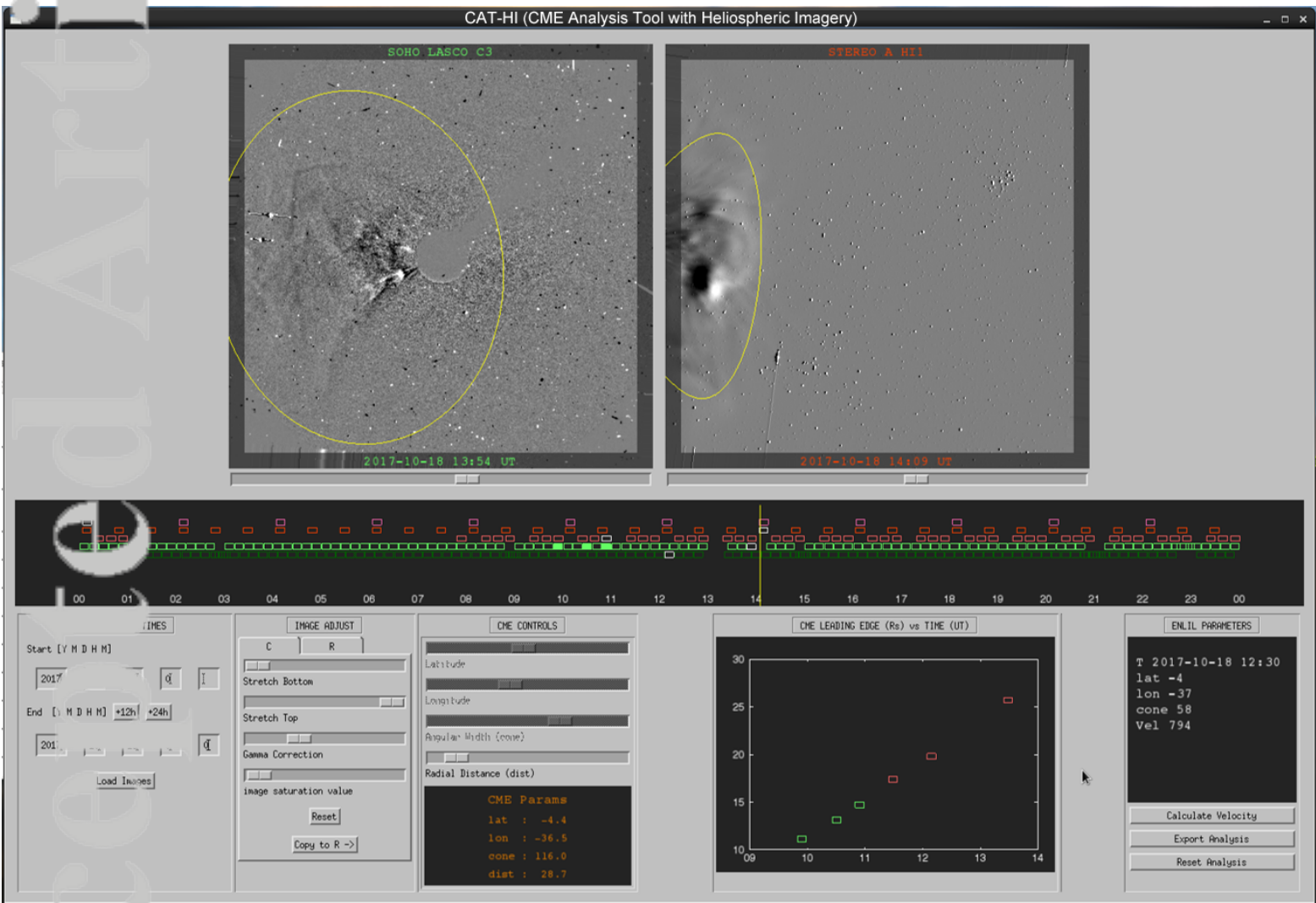


HI-2: Flat Image Position Error

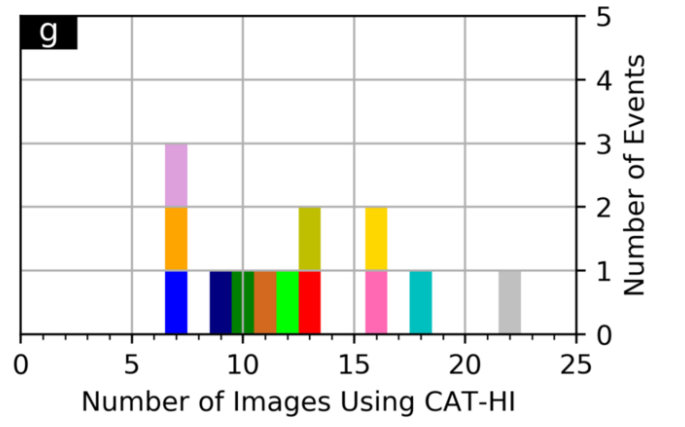
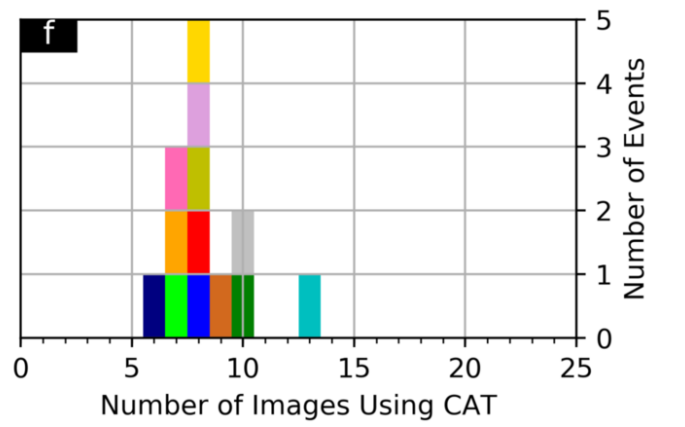
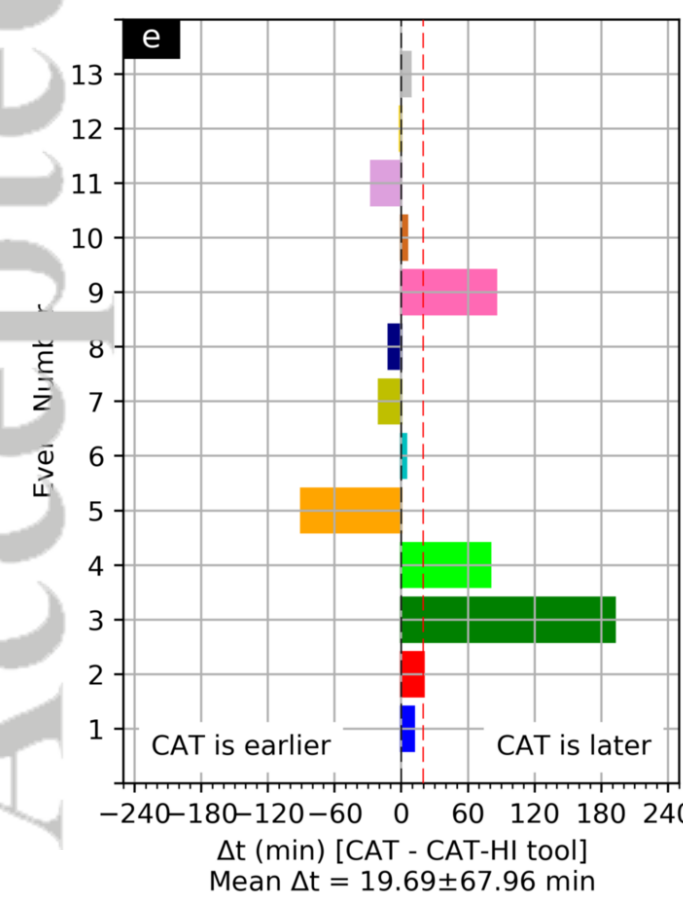
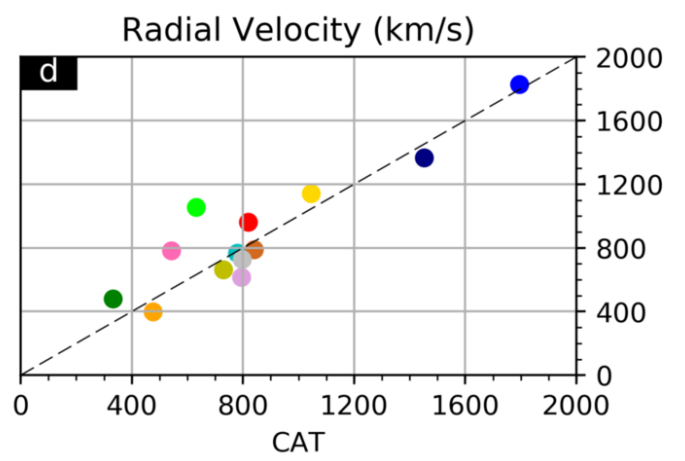
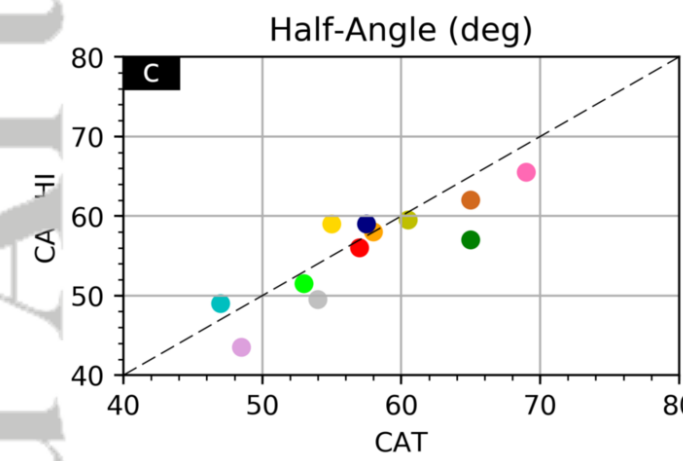
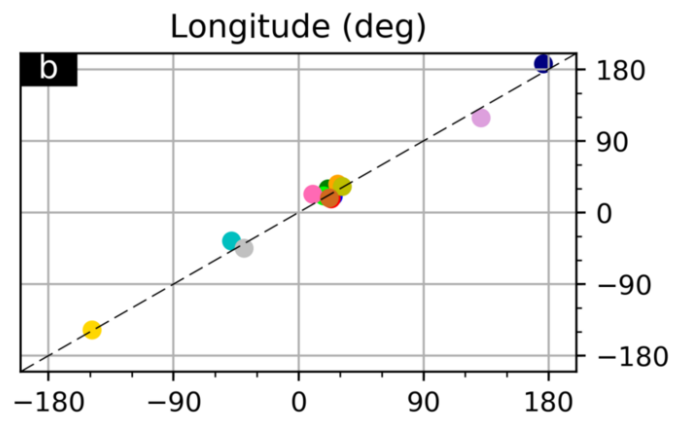
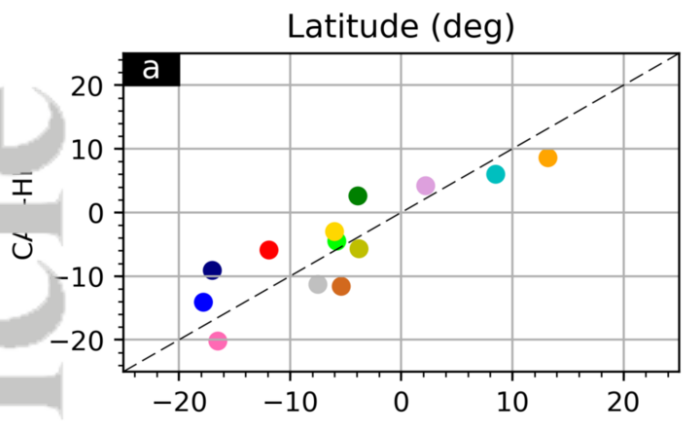




2019SW002166-f01-z-.png

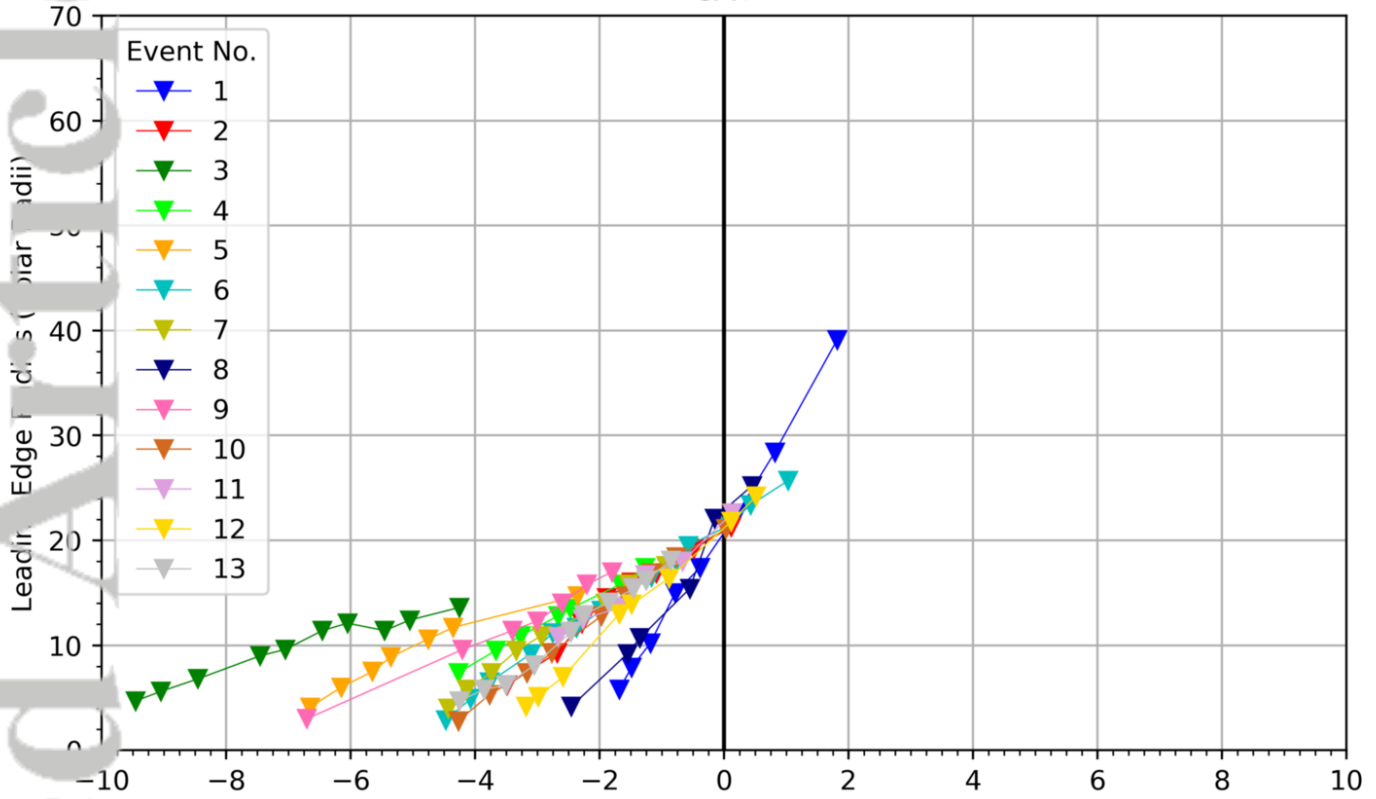


2019SW002166-f02-z-.png

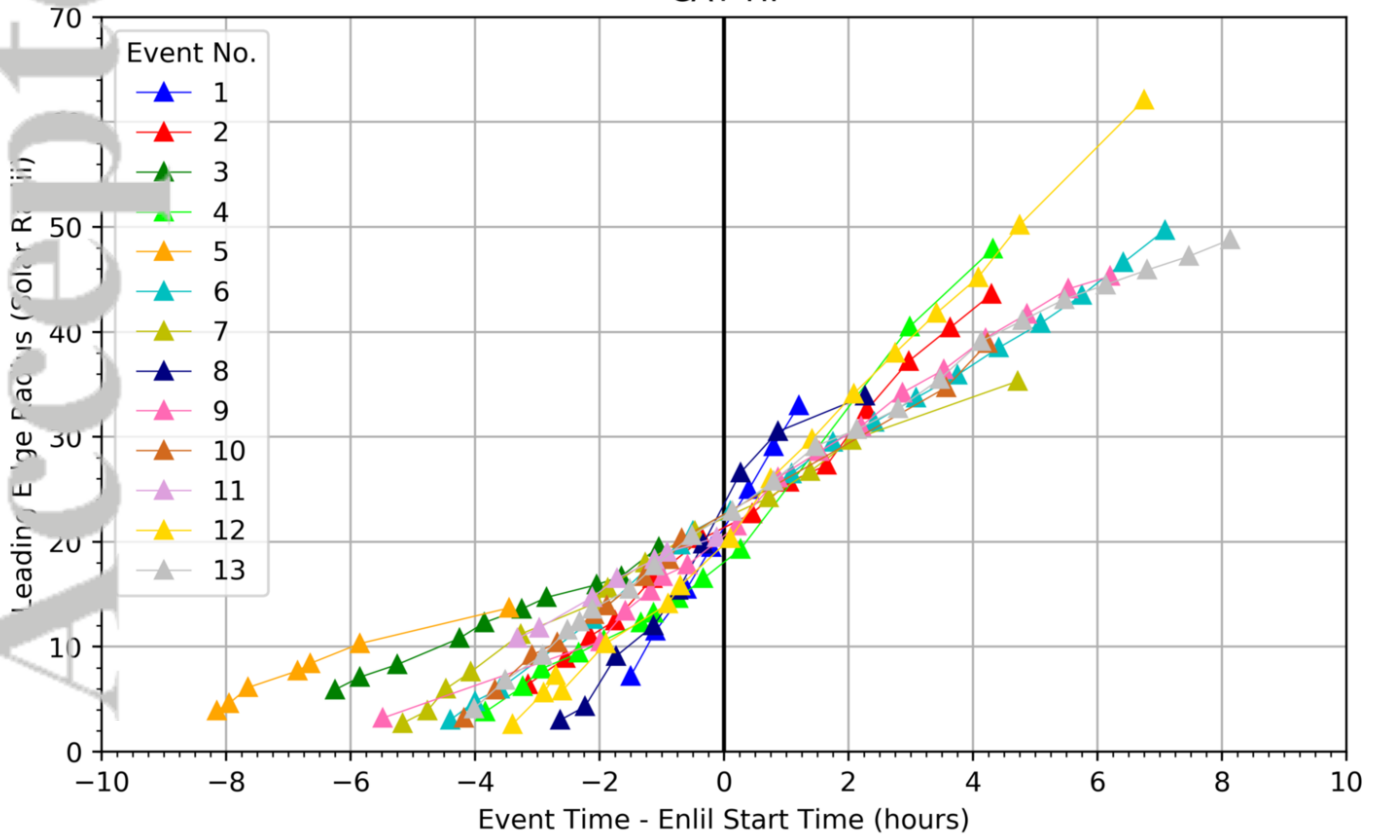


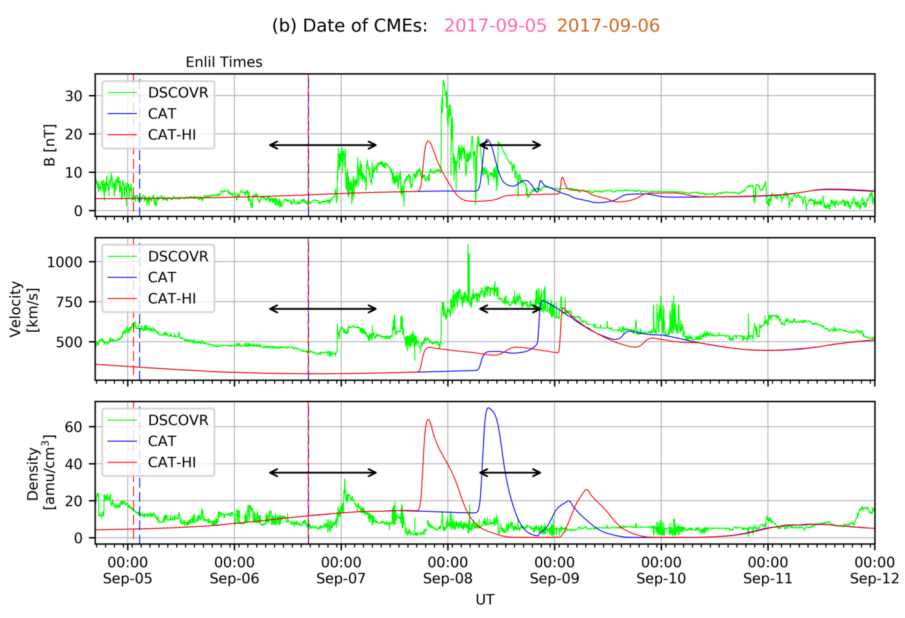
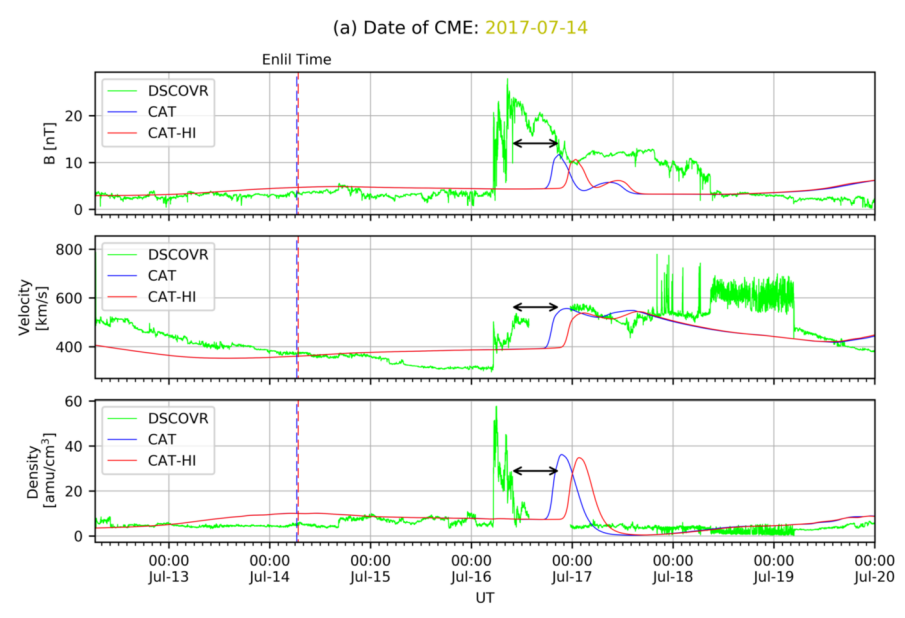
Leading edge of CME vs. Time

CAT

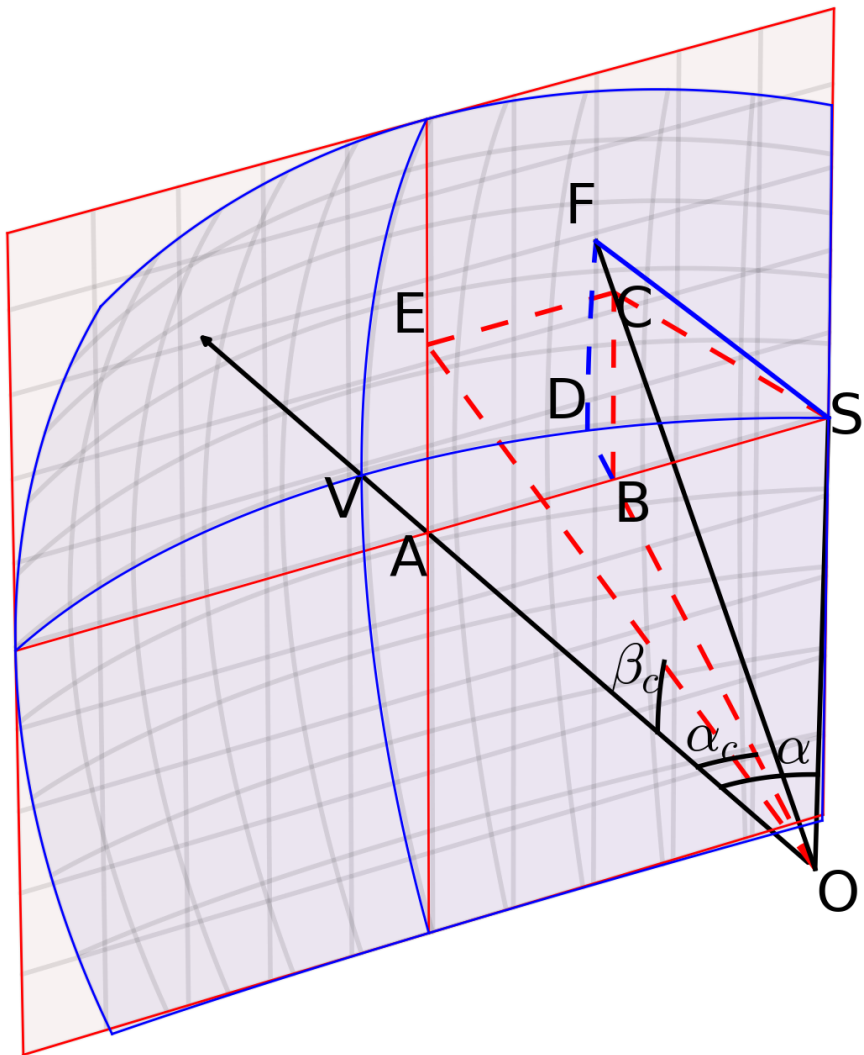


CAT-HI

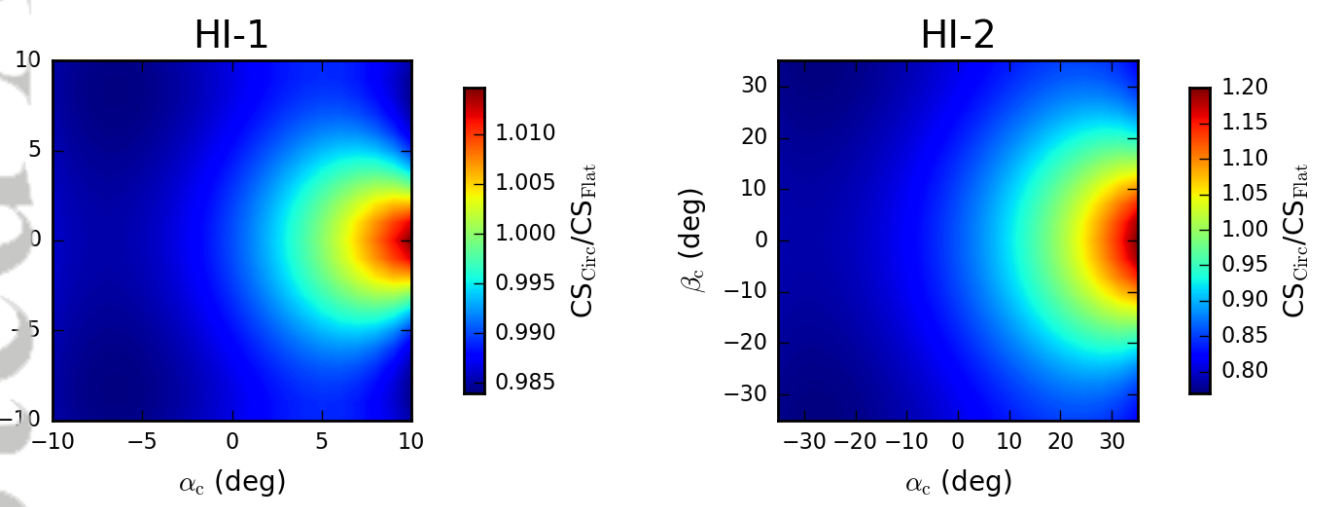




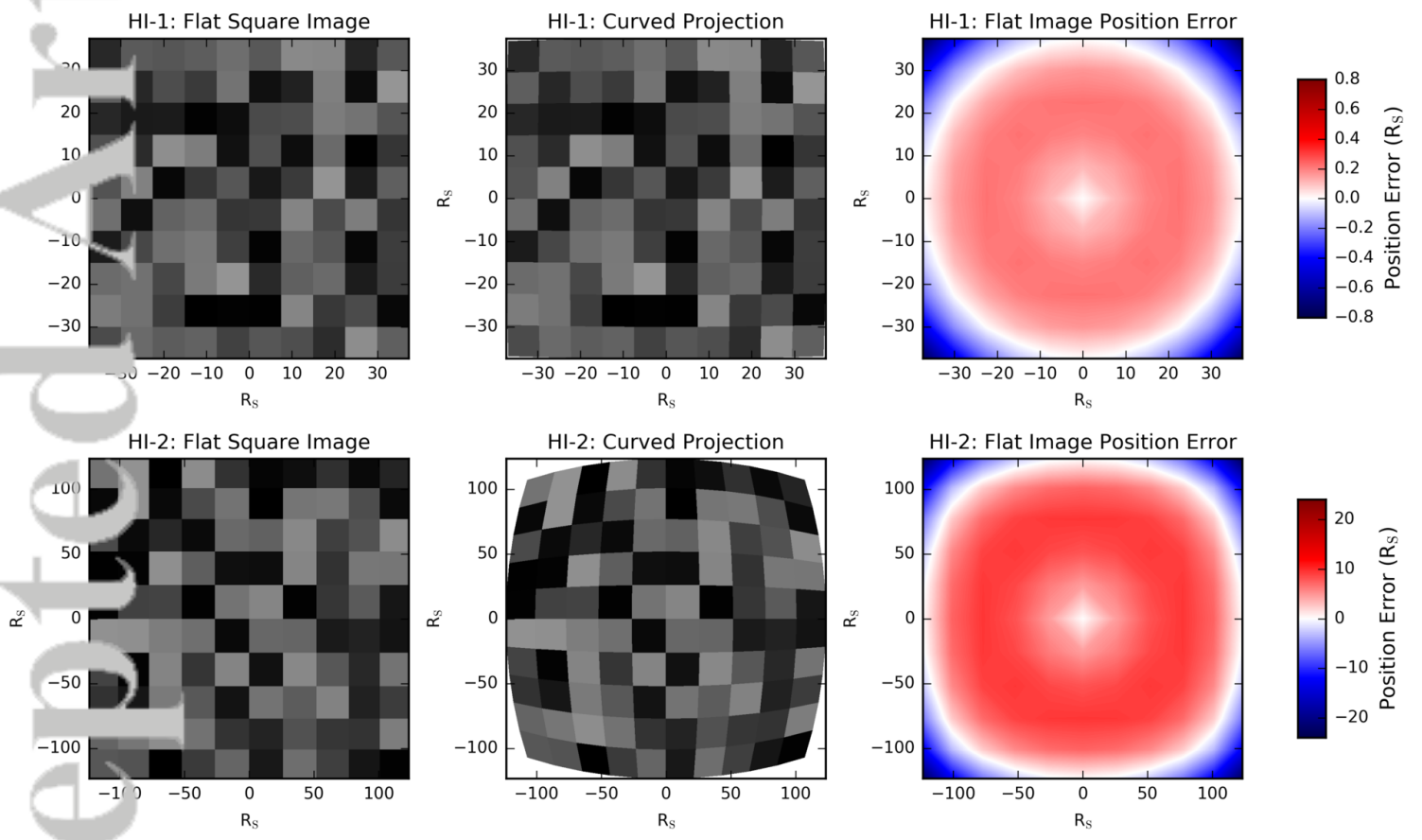
2019SW002166-f05-z-.png



2019SW002166-f06-z-.png



2019SW002166-f07-z-.png



2019SW002166-f08-z-.png